

Developing AntBot: Visual Navigation based on the insect brain

Robert Mitchell

Master of Informatics
Informatics
School of Informatics
The University of Edinburgh
April 5, 2018

Supervised by
Dr. Barbara Webb

Acknowledgements

I would like to take the opportunity to thank my supervisor, Dr. Barbara Webb, for her guidance, and invaluable insight on the subject matter. I would also like to thank the insect robotics group, in particular Jan Stankiewicz, for helping me use and understand the Vicon motion capture system used to gather results, as well as helping me talk through many problems throughout the project. My gratitude also extends to Zhaoyu Zhang and Leonard Eberding, two of my predecessors on this project; both have been extremely useful in explaining the existing codebase and operations of the robot where they were not always clear. Finally I should like to thank my parents, for their unwavering support throughout my education; I could not have made it here without them.

Declaration

I declare that this dissertation was composed by myself, the work contained herein is my own except where explicitly stated otherwise in the text, and that this work has not been submitted for any other degree or professional qualification except as specified.

Robert Mitchell

Abstract

We investigate here the process by which desert ants (*Cataglyphis Velox*) perform visual route navigation. A model proposed by Ardin *et al.* [2] has shown promise in simulation and has been implemented on AntBot, an autonomous robot designed to test the proposed navigational models for ants. This model replicates the structure of the Mushroom Body neuropils, a structure present in the brains of all insects. The mushroom bodies are known to be used primarily for olfactory learning and association. However, the increased size of the structure in the brains of hymenoptera suggests that this part of the brain may perform more complex associative tasks. One such task is visual route memory. Ardin *et al.* use a scanning route following behaviour, whereby the simulated ant scans a 60° arc and chooses the most familiar direction, to demonstrate the plausibility of their model. Previous implementations of the MB model on AntBot which use a scanning behaviour have struggled to replicate the simulation performance of Ardin *et al.*, requiring multiple corrections per run to allow the robot to reach its goal. We demonstrate the problems with the model in its current form on the robot and show how our solutions can improve the performance while remaining biologically plausible. As part of this work, we also investigate biologically plausible methods of visual collision avoidance using optical flow. Optical flow is the projection of 3D motion vectors in a scene onto a 2D image frame; the vectors which describe the motion present in an image. We present two distinct models; one based on time-to-contact and image depth [9, 12], the other using an optical flow filter [13, 11]. We demonstrate that a simple filter-based visual collision avoidance model can provide robust performance in a cluttered environment. We also demonstrate that a time-to-contact model is impractical on the current AntBot platform and propose our solutions to the problems inherent in the current model. We present our interpretation of experimental results for both the improved Mushroom Body model, and the trialled collision avoidance systems. Finally, we present our thoughts on the work carried out, suggest future development ideas, and improvements which could be made.

Contents

List of Figures	ix
List of Tables	xiii
1 Introduction	1
1.1 Motivation	1
1.2 Goals	1
1.3 Results	3
2 Background	5
2.1 Optical Flow	5
2.2 Optical flow models for Collision Avoidance	5
2.2.1 Time-to-Collision	5
2.2.2 Filtering	7
2.3 The Mushroom Body for Visual Navigation	7
2.4 The Willshaw Network	10
3 Platform	13
3.1 Hardware	13
3.2 Software	14
3.2.1 Android	14
3.2.2 Arduino	15
3.3 Modifications	15
4 Methods	17
4.1 Optical flow models for Collision Avoidance	17
4.1.1 Time-to-Collision	17
4.1.2 Filtering	18
4.2 The Mushroom Body	22
4.2.1 Real Weightings	24
4.3 AntBotStats	25
5 Experimentation	27
5.1 General	27
5.2 Collision Avoidance	27
5.3 Visual Navigation	29
6 Results and Evaluation	33
6.1 Collision Avoidance	33
6.1.1 Time-to-Collision	33
6.1.2 Filtering	34
6.2 Visual Navigation using the Mushroom Body	38
7 Discussion	47
7.1 Conclusion	47
7.2 Future work - Potential developments for MInf Part 2	47
7.2.1 Improvements on work presented	47
7.2.2 Engineering	49

8 References	51
A Visual Navigation trajectory plots	53
A.1 AB Runs	53
A.2 MAB Runs	57

List of Figures

1	The TTC model: (Caption from <i>Low and Wyeth</i> Figure 1): Time To Contact Figures: Left - Robot on a straight collision course with object, Right - Robot not on a collision course with object.	6
2	The OF filter model: (Caption from <i>Stewart et al.</i> Figure 7): Collision avoidance (CA). (A)The CA filters used in the model. Each covers 105 deg. of azimuth but they are centred at ± 3 deg. (elevation = 0 deg.). [Left and right filters are blue and red respectively.] (B) Control diagram for collision avoidance. Only the half of the system that triggers rightward saccades is shown for clarity; the other half has an identical configuration. The dark blue box represents the blue wide-field filter in A. The reset operation also applies to the other half of the system, i.e. a saccade in one direction sets both accumulators to 0. Thresh., threshold; ang. vel., angular velocity.	7
3	The Mushroom Body circuit: (Caption from <i>Ardin et al.</i> Figure 2): Images (see Fig 1) activate the visual projection neurons (vPNs). Each Kenyon cell (KC) receives input from 10 (random) vPNs and exceeds firing threshold only for coincident activation from several vPNs, thus images are encoded as a sparse pattern of KC activation. All KCs converge on a single extrinsic neuron (EN) and if activation coincides with a reward signal, the connection strength is decreased. After training the EN output to previously rewarded (familiar) images is few or no spikes.	9
4	The original network figure (Fig. 4) from <i>Willshaw et al.</i> [5].	10
5	Our modified Willshaw network which models the Mushroom Body circuit. The input (KC_{in} / N_b) represents a pattern of KC activation. The synapses represent the weight of the connection between each KC and the EN. The output represents the output of the EN.	11
6	The Kogeto Dot 360° panoramic lens.	13
7	A sample of the view given by the lens before any processing.	13
8	AntBot pre (top) and post (bottom) hardware upgrade. We can now charge AntBot directly. Note the addition of motion capture tracking markers for the Vicon system.	16
9	The filter implemented by <i>Scimeca</i> : (Caption by <i>Scimeca</i> , Figure 13): Figure (a) shows the idea behind the modification of the filter for speed retrieval. When moving forward, for example, we expect the rectangular 360 [degree] image to have vector flows in different length throughout the frame, in the pattern shown in the Figure. Figure (b) shows the filter response of the modified filtering process for this [<i>Scimeca's</i>] project. During matching, the found flow vectors will be projected onto the corresponding filter vectors nullifying the information on the y axis and scaling the vectors differently depending on the area of the image they are found in.	21
10	The erroneous familiarity pattern displayed by the network. The plot shows the familiarity response of the Extrinsic Neuron (y-axis) against the index of the scan (x-axis). 0 denotes the leftmost direction, 15 directly ahead, and 30 the rightmost direction. This was a simple plot produced early in the debugging process, hence the lack of axis labelling and higher number of scan points.	23

11	The expected familiarity response of the Extrinsic Neuron. Note the improved range of the response along with the clearly defined minimum.	23
12	The empty experimental arena.	27
13	An example of the tussocks used during experiments.	28
14	The arena used for basic tussock interaction	28
15	Arena 4. One tussock per quadrant.	29
16	Arena 5. Two tussocks per quadrant.	30
17	Arena 6. Three tussocks per quadrant.	30
18	The autoscaled plot for run MAB-5-2.	31
19	The set-scale plot for run MAB-5-2; forcing the axes to a uniform scale over all runs gives a more accurate immediate view of the runs and their similarity.	32
20	$\pm 45^\circ$ offset image frames showing the flow vectors computed at each point (distinct black pixels). The five images were taken over the course of one minute while the robot was stationary in G.17.	33
21	The appearance of the tussock in the visual frame (boxed in red). Though the tussock is completely obstructing the frontal section of the robot's view, the tussock is comparatively small in the visual frame. This image was taken without the enclosure.	35
22	Arena 7. The diagonal wall arena.	36
23	Arena 8. The curved wall arena.	37
24	Arena 9. The fluted walls arena.	37
25	Trajectory plot of run AB-4-1; this run was considered a failure of the Visual Navigation system.	42
26	Trajectory plot of run AB-3-1; this run was considered a success of the Visual Navigation system.	42
27	Trajectory plot of run AB-1-2; a near-successful recovery.	43
28	Trajectory plot of run AB-1-2; a failed recovery.	43
29	Trajectory plot of run AB-3-2.	44
30	Trajectory plot of the homeward experiment. The Vicon capture was accidentally stopped early during outward trip <i>Memory 4</i> and the last section of the trip was missed. The linkage has been filled in to show where the rough route the robot took but it must be understood that this is not part of the recording, the line was simply drawn to fill in the gap.	45
31	Run AB-1-1.	53
32	Run AB-1-2.	53
33	Run AB-2-1.	54
34	Run AB-2-2.	54
35	Run AB-3-1.	55
36	Run AB-3-2.	55
37	Run AB-4-1.	56
38	Run AB-4-2.	56
39	Run MAB-1-1.	57
40	Run MAB-1-2.	57
41	Run MAB-2-1.	58
42	Run MAB-2-2.	58
43	Run MAB-3-1.	59
44	Run MAB-3-2.	59
45	Run MAB-4-1.	60
46	Run MAB-4-2.	60

47	Run MAB-5-1.	61
48	Run MAB-5-2.	61

List of Tables

1	The available commands on the Arduino and the messages sent to invoke them. Those values which are changeable are shown in italics. The <i>go</i> command was added by <i>Scimeca</i> . This table was adapted from [6, 11].	15
2	The results for the functional performance experiments on the filtering CA system. (*) This was the only case of a risk on end coming from a tussock during formal experiments, all other potential collisions were with the side of the arena. (**) The first turn the robot made took it away from the arena in the manner described in 5, the collision was with the arena wall in the South East corner as the robot had no where left to go.	34
3	The results for the behavioural experiments conducted on the optical flow system; for these, arenas were designed to elicit a certain behavioural response, however, they mostly failed to do so, highlighting problems with the current implementation and methods of experimentation. The “As expected” column denotes cases whether the robot performed the expected moves: No means not at all, Almost means that movements were initially correct then went wrong, and Yes means complete success.	36
4	The summarised results for the VN experiments. All distances are given in millimetres. The green and red distances correspond to the distances marked in green dashes and red dashes on the plots. Distance taken denotes the distance used to determine success; N/A was given in the case where neither measure was more meaningful than the other. For an explanation of interpretation, please see the results discussion for VN experiments. (*) While we consider this run a success, the memory route does deviate significantly from the learned route though it seems correction is attempted. (**) These are considered edge cases, by our interpretation they are successes, however they could also be considered failures (particularly MAB-4-1). This table was copied by hand; in the case the distances presented disagree with the distances on the plots, the plots prevail. We count a 77% success rate including edge cases, 66% excluding.	40

1 Introduction

Desert ants (*Cataglyphis velox*) have the remarkable ability to navigate through complex natural environments, using only low-resolution visual information and limited computational power. It is well documented that many species of ant, and other hymenoptera are capable of very robust visual navigation; however, it is as yet unclear how the insects perform this seemingly complex task with such little brainpower. In this paper, we will focus on using an existing model for visual navigation in ants using the Mushroom Body circuit, an artificial neural network which emulates the Mushroom Body neuropils in the ant brain. We will also discuss biologically plausible methods of visual Collision Avoidance using Optical Flow. We will also discuss possible extensions of this model. A robot (AntBot) has been constructed [6] to allow us a testing platform on which to implement, and experiment with, the algorithms in the *Ant Navigational Toolkit* [14].

1.1 Motivation

Though we are able to observe and mimic algorithmically the visual navigational capabilities of insects, we still do not understand the precise methods by which this process takes place. The model we will look at was proposed by Ardin *et al.* [2], which takes the Mushroom Body (whose function is thought to be primarily for olfactory learning), and shows that this provides a plausible neural model for encoding visual memories.

The MB circuit has been implemented and tested on AntBot by Eberding and Zhang respectively, however the existing MB circuit is fairly simple. It uses randomized connections between the visual projection neurons and the Kenyon Cells, and binary weightings between the Kenyon Cells and a single Extrinsic Neuron denoting the level of image recognition. A modification was made by Zhang, whereby eight ENs were used, one for each of the cardinal directions in the Central Complex model. This will be discussed further in Section 2.3. The reader should note that the Central Complex (CX) model is primarily used to model the task of Path Integration and will not be discussed further (see [11]). Previous projects did not achieve robust performance using a scanning route following strategy so we aim to establish a baseline for performance using the MB circuit with our own route following strategy.

We would also like to look at methods for collision avoidance (CA) which do not involve specialised sensors such as a LIDAR or SONAR, the luxury of which, ants do not have. Models have been proposed which use Optical Flow (OF) properties to determine whether or not a collision is imminent. These models have been proposed both in purely robotic contexts [12], and biological ones [9].

1.2 Goals

The project aims for the following experimental scenario to be possible: We want to send the robot on a run through an obstacle course, allowing it to navigate however it chooses through the environment. From here, we want the robot to be able to replicate this route using only visual memories, which it should store on that initial run. As a small extension, we would like the robot to be able to navigate home following the reverse of this route. It should be noted that this final step is not strictly accurate to

the behaviour of the desert ant. As noted by [3] in their familiarity-driven study of ant route navigation, *Wehner et al.* [15] demonstrated that the remembered routes have a distinct polarity, so knowledge of a route from nest to food, does not imply that the ant has knowledge of a route from food to nest. In this case, we make the outward and homeward route the same.

The first stage of the project will focus upon obtaining a working collision avoidance system as a pre-requisite to gathering the route information. This CA system should be based on visual information readily available to AntBot with no additional/specialist sensors. For this paper, we assume that CA is a low-level reactionary behaviour, in that, we do not use any further processing of the detected motion; we react based on the immediate stimulus of the flow field. We will look at two different optical flow techniques used to build CA systems. We will also discuss the effects of using different types of flow field and different methods of response.

We then move to the Mushroom Body circuit; this model for visual navigation was demonstrated by [2] in simulation. Previous iterations of this project which focussed on the Mushroom Body circuit have struggled to achieve similar performance on a robot using the methods originally presented by *Ardin et al.*; certainly, no previous iteration has dealt with a non-deterministic route through a cluttered environment. We aim to get the original *basic* model from [2] working on the robot in a robust fashion and hope to establish a baseline against which future projects can work while modifying the model. We will use a modified scanning behaviour to establish this baseline. Ants have demonstrated use of scanning in visual navigation but it is generally accepted that this is not the primary method they use to determine a direction after having recognised a scene, rather, this scanning behaviour only occurs in certain scenarios (e.g. when the ant becomes lost) [8]. This will require debugging of the existing model and any interacting factors; for example, *Zhang* managed to achieve good results with the MB model using klinokinesis as the route following behaviour while a scanning behaviour struggled to produce robust routes. It should also be noted that the scanning behaviour performed poorly using a Perfect Memory model [17] (the best model used by *Ardin et al.*) which suggests that the model is not the only factor that contributes to the accuracy of recapitulated routes.

Finally, we will report the results of the experiments and testing performed at different stages during, and post development; we will compare these to relevant results from previous iterations of this project. We will end with a conclusion of our findings and contributions to the project, as well as discussing technical limitations and potential for future developments.

1.3 Results

This work is based on work done previously by Leonard Eberding, Luca Scimeca, and Zhaoyu Zhang [6, 11, 17].

Significant contributions of this project:

1. An optical flow based system for Collision Avoidance,
2. Results indicating the impracticality of a time-to-contact based system for Collision Avoidance,
3. Implemented hardware upgrades to AntBot to make the platform more robust,
4. Implemented a basic but extensible statistical logging utility on AntBot with a complementary parsing and plotting utility written in Python,
5. Implemented a new type of scanning behaviour for AntBot,
6. Successful recapitulation of multiple routes through a cluttered environment using Visual Navigation.

2 Background

2.1 Optical Flow

Image flow is defined as being the 3D velocity vector of an object, projected onto a 2D image plane[10]. Optical flow is an approximation of this, working from a series of images to compute the projected velocity vector for a pixel. A single *flow vector* shows the displacement of a single pixel from one image to the next. A set of these flow vectors creates a *flow field*, a collection of vectors which describe the motion in the complete image.

Broadly, there are two types of flow field: dense and sparse (also known as differential and feature-based respectively[9]). A *dense* flow field tracks the motion of every pixel in the image. A *sparse* flow field tracks the motion of a subset of pixels in the image. The sparse field may track a uniform subset of pixels, such as a grid, or a set of important points in the image, such as the prominent features in the image (object corners). See 4 for implementation.

2.2 Optical flow models for Collision Avoidance

Collision avoidance is an important component in navigation. Ants do not have dedicated sensory systems or the ability to create a visual 3D map of their environment using stereoscopic vision or motion parallax. It has been demonstrated that optical flow is used by honeybees in performing visual navigation [4], so it is not unreasonable to think that bees and other hymenoptera may use this information for other purposes. Indeed, optical flow has been shown to be a viable model for collision avoidance in *Drosophila* [13]. We visit two models in this paper which we will term the *time-to-collision* model and the *filtering* model.

2.2.1 Time-to-Collision

This model, proposed by *Low and Wyeth*[9], aims to replicate the CA capabilities of larger animals such as birds and humans. The model relies on accurately computing the *time-to-collision* or *time-to-contact* (TTC), which is the computed time until the robot collides with an obstacle. The TTC is computed as follows:

$$TTC = \frac{r}{v} \quad (1)$$

Where r is the distance from a point object on a collision course with the robot and v is constant speed at which the robot and object are closing.

Low and Wyeth then alter this equation by taking the direction of the velocity vector v and the direction to a point on the object and computing the angle between these two vectors ϕ . Their TTC equation then becomes:

$$TTC = \frac{\cos\phi \times \sin\phi}{\phi} \quad (2)$$

The TTC is then used to generate range information (image depth), which can be used to generate an appropriate reaction.

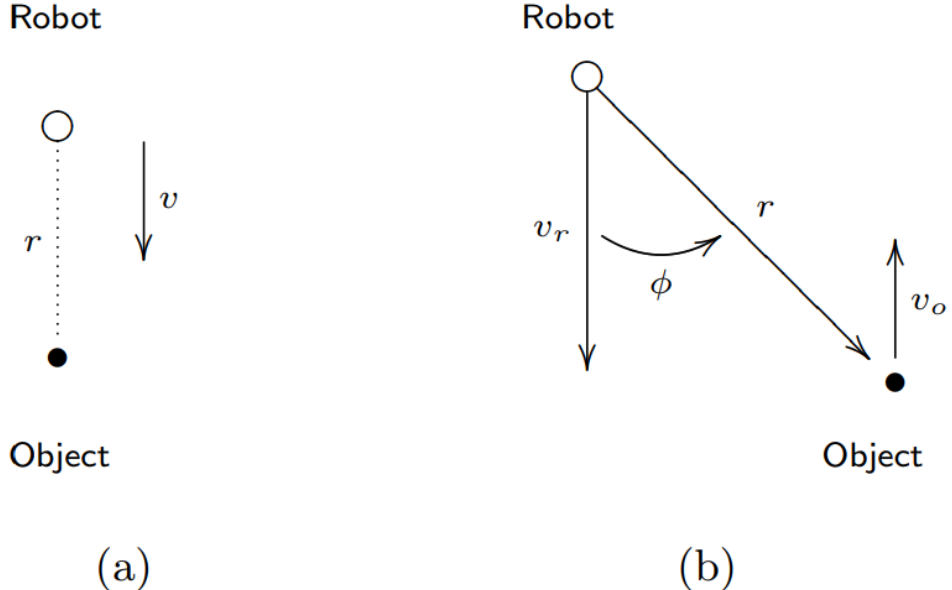


Figure 1: The TTC model: (Caption from *Low and Wyeth* Figure 1): Time To Contact Figures: Left - Robot on a straight collision course with object, Right - Robot not on a collision course with object.

An alternative, yet equivalent, method for computing the TTC is given by *Souhila and Karim* wherein the time-to-contact is given in terms of the distance of all pixels from the *focus of expansion* (FOE); the point from which all flow vectors originate. *Souhila and Karim* do not give a method of explicitly computing the FOE of a flow frame however, they do describe their method of estimating it. All flow vectors are in two dimensions with a horizontal (x) and vertical (y) component. Focussing on the horizontal case; flow vectors to the right of the FOE will have a positive x component, and flow vectors to the left of the FOE will have a negative x component. They then tally the signs of the horizontal components of the flow vectors computing a difference between the horizontal components on the left of the FOE, and the horizontal components on the right of the FOE. Intuitively, at the point where this difference is minimised, the divergence of the horizontal components is maximised; this gives us the horizontal component of the FOE. The vertical component is computed in a similar manner.

Finally, they compute the TTC as:

$$TTC = \frac{\Delta_i}{|\vec{V}_t|} \dots \quad (3)$$

Where Δ_i is the distance of a point $p_i = (x, y)$ from the FOE, and $|\vec{V}_t|$ is the translational velocity of the camera computed from optical flow[12].

This time-to-contact is then used to compute image depth information and a reaction is generated based on the magnitudes of the vectors surrounding the FOE. The reaction is controlled by the image depth information as well as a “balance strategy”. The balance strategy steers the robot away from the side of greatest flow, but keeps the robot within its designated navigational zone (governed by the depth information). The balance strategy is similar to the filtering system described in Section 4, though the explicit method used by *Souhila and Karim* is not explored in this project.

2.2.2 Filtering

The filtering method asks the following question: Given my current motion, what visual changes do I expect to see? Much of the following explanation was provided by [13]. A model proposed by *Stewart et al.* for CA in simulated fruit flies takes advantage of the fact that expanding patterns will trigger an avoidance manoeuvre away from the focus of expansion[13]. Their model uses two offset flow filters (the *expected flow*). Each filter is constructed as a frontally centered expansion pattern with the same spatial extent to either side of the expansion pole (the central vertical axis of the pattern). These filters are then offset by $+3^\circ$ for the right and -3° for the left. The left and right filters feed into leaky accumulators, and if the accumulator exceeds a given threshold, a saccade in the opposite direction is triggered. The model from [13] is shown in Figure 2. We discuss a modified version of this model in section 4.

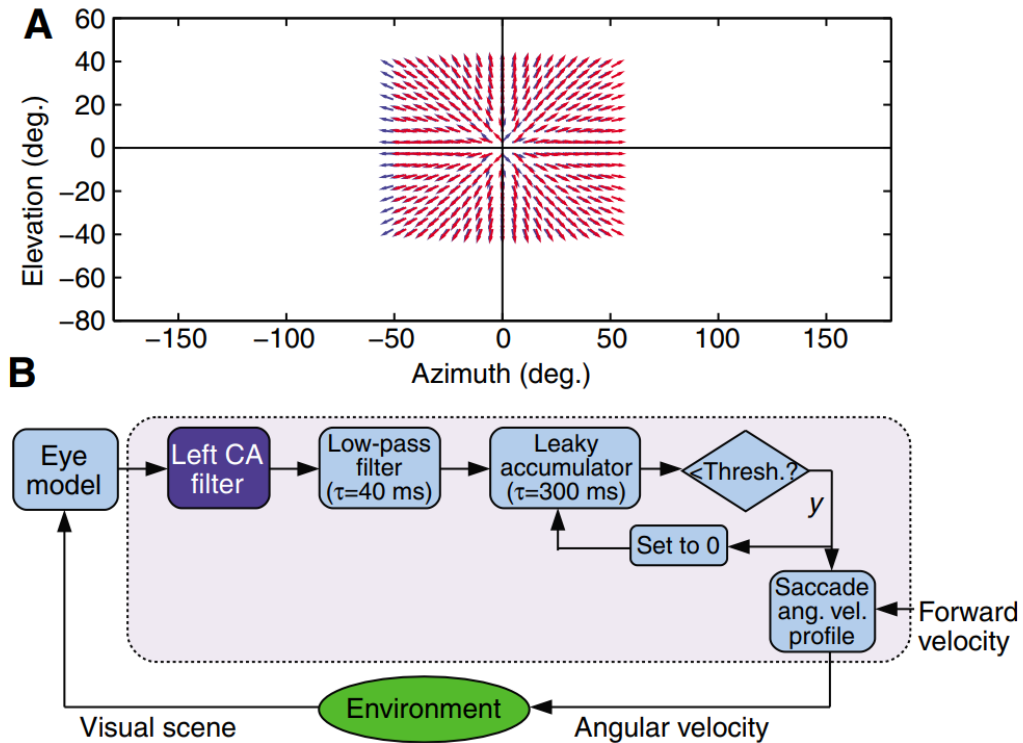


Figure 2: The OF filter model: (Caption from *Stewart et al.* Figure 7): Collision avoidance (CA). (A)The CA filters used in the model. Each covers 105 deg. of azimuth but they are centred at ± 3 deg. (elevation = 0 deg.). [Left and right filters are blue and red respectively.] (B) Control diagram for collision avoidance. Only the half of the system that triggers rightward saccades is shown for clarity; the other half has an identical configuration. The dark blue box represents the blue wide-field filter in A. The reset operation also applies to the other half of the system, i.e. a saccade in one direction sets both accumulators to 0. Thresh., threshold; ang. vel., angular velocity.

2.3 The Mushroom Body for Visual Navigation

The Mushroom Body neuropils are structures present in the brains of all insects though they are largest in the brains of hymenoptera. They are known to play a critical role in olfactory learning, and have been thought to play a role in visual memory in

hymenoptera since 1982 at the latest[1]. In 2016 a Mushroom Body circuit was proposed by *Ardin et al.* to allow emulation of the structure in a simulated desert ant [2]. The simulated ant's view is taken from 1cm above the ground and has a field of view of 296° azimuth by 76° elevation. A ratio of $4^\circ/\text{pixel}$ is used to give a 19×74 pixel image. This image is then downsampled to 10×36 pixels to give a realistic resolution for ant vision. A 1×360 vector is used for further processing.

The generalised MB circuit is a three layer neural network: The first layer consists of a set of visual Projection Neurons (vPNs), these connect to the second layer of standard artificial neurons referred to as Kenyon Cells (KCs), and finally these KCs connect to a set of Extrinsic Neurons (ENs). The reader should note that any reference to the weight of a Kenyon Cell herein is refers specifically to the weight of the connection between that KC and the Extrinsic Neuron; this abstraction is made for ease of reference.

The model by *Ardin et al.* (shown in Figure 3) consists of 350 vPNs (one for each pixel in the downsampled image). In the second layer we have 20,000 KCs each of which receives input from 10 randomly selected vPNs; each KC requires coincident input from multiple vPNs to fire. Every KC is then connected to a single EN which sums the number of KCs which are activated by the input image. The network is trained by providing a reward signal at regular intervals. If KC activation coincides with a reward signal, the connection strength to the EN is greatly reduced. The single EN simply gives an unfamiliarity measure for the image seen. The agent decides on its next action by scanning to find the direction of greatest familiarity.

This version of the MB circuit has demonstrated the capacity to learn scene information, as well as recapitulate routes by using the scanning technique [2]. In 2016, *Eberding* implemented the Willshaw Network (WN) on AntBot, which resembles the Mushroom Body circuit (see Section 2.4); he demonstrated that the network allowed the agent to perform visual navigation through a sparse testing environment[6]. The agent navigates by scanning, computing unfamiliarity, and finally choosing the direction of minimum unfamiliarity. In order to save on computational resources, the KCs are binary rather than spiking (we hope to explore a spiking model in the future). While this does generate a correct route, it is not as continuous as those performed by real ants.

In 2017, *Zhang* implemented a route following strategy originally proposed by *Koszhabashev and Mangan* which employed klinokinesis in place of scanning. Klinokinesis is one of two main forms of kinesis - the movement of an organism in response to stimulus - in which the turning rate is proportional to stimulus intensity. In [17], the stimulus is given by the unfamiliarity metric generated by the MB model. The step size between each turning point as well as the turning angle depends on the unfamiliarity of the current view. The same algorithm from [8] is used to perform klinokinesis on the robot.

A separate model, also implemented by *Zhang*, added seven extrinsic neurons. Each EN is then used to represent one of eight directions relative to the robot's current heading; if we take 0° to be the robot's forward direction then the other seven directions correspond to $+45^\circ$, $+90^\circ$, $+135^\circ$, $\pm 180^\circ$, -135° , -90° , and -45° . This model was implemented as a way of combining the MB model for visual navigation and the CX model for path integration. While path integration and the CX model are not explored in this project, the model is still worth discussing as it may still be used to encode a

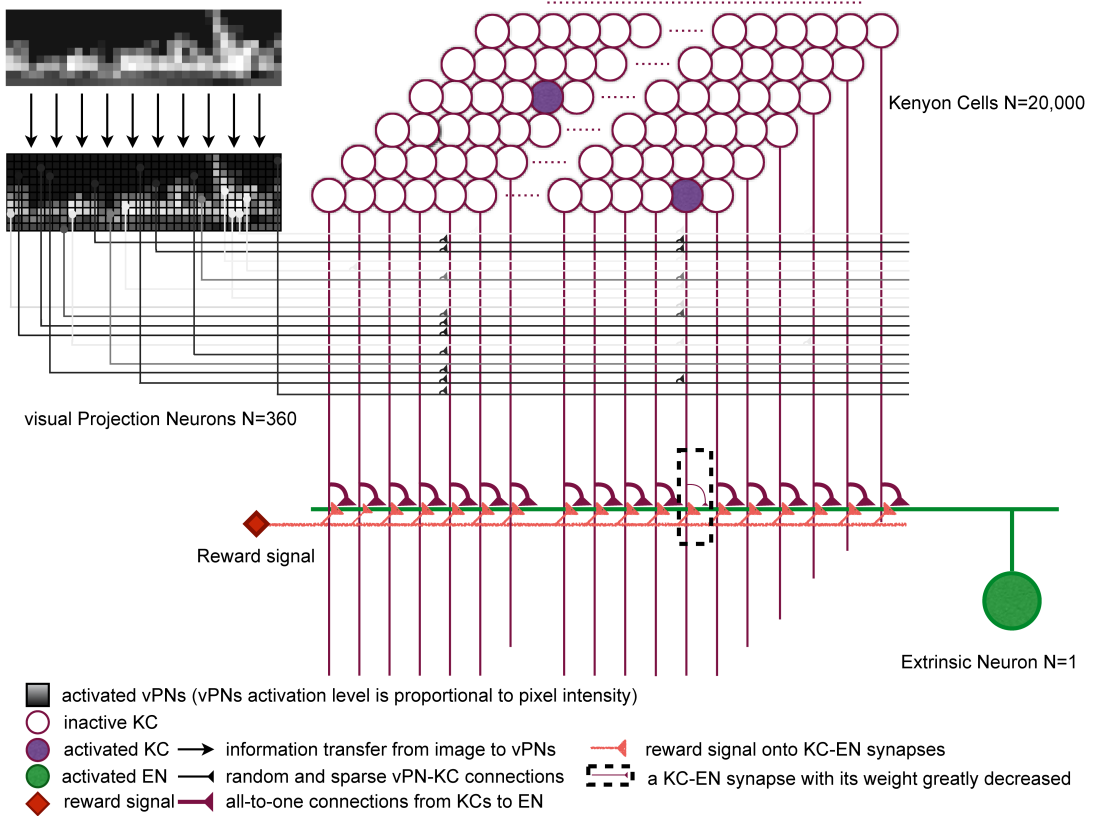


Figure 3: The Mushroom Body circuit: (Caption from Ardin *et al.* Figure 2): Images (see Fig 1) activate the visual projection neurons (vPNs). Each Kenyon cell (KC) receives input from 10 (random) vPNs and exceeds firing threshold only for coincident activation from several vPNs, thus images are encoded as a sparse pattern of KC activation. All KCs converge on a single extrinsic neuron (EN) and if activation coincides with a reward signal, the connection strength is decreased. After training the EN output to previously rewarded (familiar) images is few or no spikes.

desired response to specific stimuli.

2.4 The Willshaw Network

The Willshaw network is a type of associative neural network with an interesting background; capable of instantaneous learning and high capacity. Coincidentally the Willshaw net mimics the structure of the Mushroom Body inputs, storage layer, and outputs.

The idea behind the network stems from the effect of passing a pattern of light beams through two patterned pinhole cards and a lens to create a pattern of refraction on a screen. The pattern output on the screen is said to be a correlogram patterns on the cards. Intuitively, the light pattern output at A can be passed through filter pattern B to produce pattern C . This idea is then refined by *Willshaw et al.* into a simple, three-layer neural network. As an aside, though the terminology of artificial neural networks is not used in the original paper, the model presented is designed to be interpreted as a biological neural network, so interpretation as an ANN is a case of semantics. The three layers of the Willshaw network are quite simple: a set of input neurons N_B are represented as parallel horizontal lines; a set of output neurons N_A are represented as parallel vertical lines; and finally the storage layer is a map of all of the intersections between the inputs and outputs. The storage layer is made up of artificial synapses which are initially inactive (weight zero). The synapses are activated (weight set to one) when the input pattern and output pattern activate the same synapse. More succinctly, synapse $c_{i,j}$ is set to 1 when a_i and b_j are activated simultaneously.

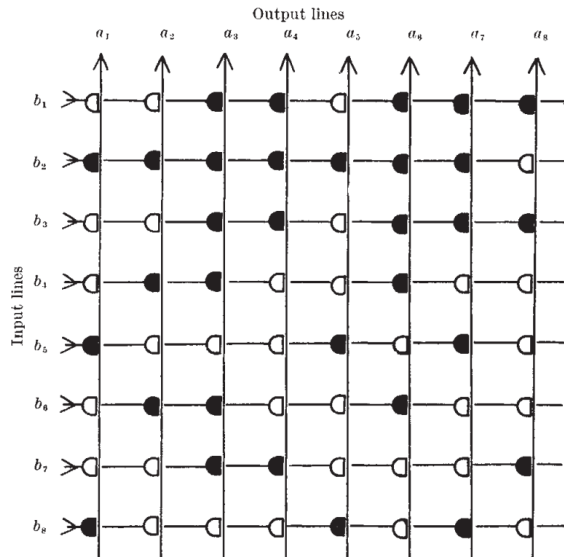


Fig. 4. An associative net.

Figure 4: The original network figure (Fig. 4) from *Willshaw et al.* [5].

This network can be transformed into something which models the MB circuit presented by [2](shown in Figure 5). Each input line represents the activity of a single KC in the network. A KC is “active” when its aggregate input from the linked vPNs is greater than a set threshold. Thus, the input to the network represents a pattern of KC activation. The synapses represent the weight of the connection between each KC and the output line (EN). We reduce the network to a single output representing the unfamiliarity measure returned (i.e. the sum of the weights of the KCs activated in the

input pattern). We make one slight tweak in adding a *reward* signal. In our version, learning only occurs in the presence of the reward signal. Learning is otherwise identical to the original model though the weighting convention for the synapses is reversed (0 is now “active”, 1 “inactive”). Adding more ENs simply means adding more vertical components to the model.

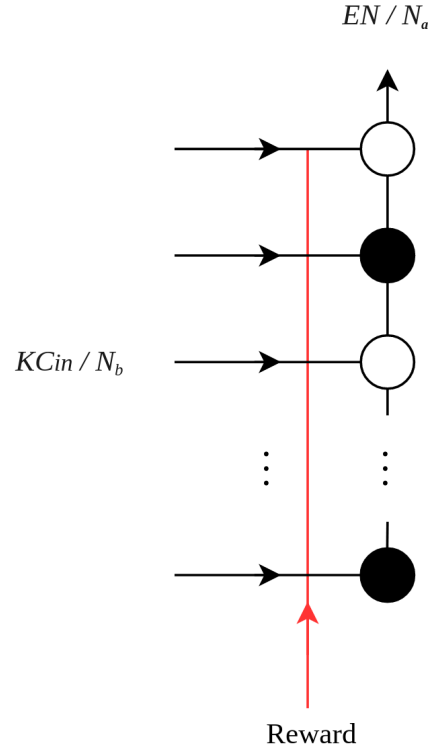


Figure 5: Our modified Willshaw network which models the Mushroom Body circuit. The input (KC_{in} / N_b) represents a pattern of KC activation. The synapses represent the weight of the connection between each KC and the EN. The output represents the output of the EN.



Figure 6: The Kogeto Dot 360° panoramic lens.



Figure 7: A sample of the view given by the lens before any processing.

3 Platform

In order to test the hypothesised models for ant navigation we use a simple autonomous robot - AntBot. AntBot was originally developed by *Eberding* in 2016; here we will discuss his design and implementation, upon which we develop our algorithms.

3.1 Hardware

AntBot's predecessor, Roboant, was originally designed by *Kodzhabashev* [7] as a compact Android robot. The robot required only four components: A sufficiently powerful Android phone (A Google Nexus 5 was used) as the brain, the Zumo Robot shield by Pololu as the chassis, an Arduino microcontroller to allow them to communicate, and finally a 360° camera attachment. AntBot uses the same basic structure, however, a Dangu 5 Rover chassis is used as the base, and therefore an alternate motor controller board is used.

The Android phone was chosen as the control module for the robot for a number of reasons. Firstly, the hardware; a modern smartphone allows a compact, powerful platform on which to build the software system as well as providing built in sensory systems and the libraries to use them (e.g. the camera). The Google Nexus 5 is more than capable of running image processing software, analysing optical flow patterns, and simulating the required artificial neural networks required for this project. Using an Android platform also allows for modular software design (see Section 3.2.1). In order to mimic the near 360° field of view (FOV) given by the ant's compound eyes, we use a panoramic lens (the Kogeto Dot), which uses a convex mirror to give a full 360° FOV. This lens is attached to the front camera and requires some pre-processing to retrieve the desired 360×40 image. As with Roboant, the Android phone is connected to an Arduino using a serial interface. Commands are sent from the phone to the Arduino which then executes the relevant commands on the motor board to provide motion control.

3.2 Software

3.2.1 Android

The architecture of the Android operating system is such that applications can (subject to certain constraints) run in parallel while broadcasting important information to one another. This allows for a modular, ROS-like¹ system in which we can have a dedicated application for each navigational subsystem employed by AntBot.

In this fashion, *Eberding* implemented an Android Application Network (AAN) consisting of five applications:

1. The *AntEye* application - This application is the main application in the network and provides the user interface, along with all camera interaction and visual processing. To summarise; the visual processing system takes the 360° panoramic image from the camera, extracts the blue channel information, crops out the ring which contains the actual image and reshapes this into a $360 \times 40px$ image, and finally downsamples this to a $90 \times 10px$ image. This final image is then used by any application which requires visual information.
2. The *Path Integration* application - This application is responsible for performing all tasks related to Path Integration (PI). PI is the process of computing displacement based on a series of consecutive moves. In *Eberding's* original implementation this application did not perform PI, but was instead used as a utility application to record orientation and distance travelled. *Scimeca* extended this application to implement PI, using both a mathematical and neural approach.
3. The *Visual Navigation* application - Similar to the PI application, the VN application houses the necessary components for performing visual navigation tasks. *Eberding* implemented both the Willshaw (Mushroom Body) network, and also a Perfect Memory (PM) module both of which were extended by *Zhang*. There also exists a super-class for visual navigation algorithms.
4. The *Combiner* application - This application is used to combine the output from the VN and PI applications in order to compute what action the robot should take. This application governs the movement of the robot based on the two primary navigational systems.
5. The *Serial Communications* application - This application governs all communication from the Android phone to the Arduino and server-interface. Android forbids multiple applications from using a single serial or Wifi port, so this application was developed as an intermediary to allow the other applications in the network to communicate through a single application.

Eberding's implementation included a server interface which was used to control the robot remotely using the phone's Wifi hotspot and Serial Communicatin App, however, this interface has not been used since the original implementation. For more information, please see [6]. It should also be noted that, due to work conducted during previous iterations of this project, it may not be possible to follow this exact structure.

¹Robot Operating System - ROS: <http://www.ros.org/>

Command	Message	Action
Heartbeat	$x \text{ seconds } n$	Feedback sent to verify a stable connection between the phone and the Arduino. A signal is sent every second with a timestamp and checked.
Move	$t \text{ 0 } distance \text{ n}$	Travel a set distance in metres.
Turn	$t \text{ 0 } angle \text{ m 0 } n$	Turn a set angle (in degrees).
Turn and Move	$t \text{ angle } m \text{ distance } n$	Turn by a specified angle then move the specified distance.
Turn left	l	Turn left indefinitely.
Turn right	r	Turn right indefinitely.
Halt	h	Stop any command in progress and stop the robot.
Go	$g \text{ leftSpeed } rightSpeed \text{ n}$	Move indefinitely with specified left and right speeds.

Table 1: The available commands on the Arduino and the messages sent to invoke them. Those values which are changeable are shown in italics. The *go* command was added by *Scimeca*. This table was adapted from [6, 11].

3.2.2 Arduino

The Arduino software is split into two sections: the *parser* and the *executioner*[6]. The parser will receive commands from the serial port and convert them into a series of movement commands. These movement commands are then sent to the motor board by the executioner. Encoder information may be gathered by the Arduino and sent back to the phone for processing. For this project, the Arduino code has not been modified. We only required the use of two commands for this project; *go*, which allows the robot to move indefinitely at a set speed, and *turn*, which allows the robot to turn to a desired (relative) angle. The *go* command also allows the operator to specify a speed for the left and right sides allowing the robot to move in smooth arcs. A full list of commands can be seen in Table 1.

Previous works have mentioned a message of the format $e \text{ e1 e2 e3 e4 } n$. This message was used to send wheel encoder information from the Arduino to the phone, however, this message was only sent during the execution of a particular function and it has since been removed from the Arduino code. There are currently no utilities available to retrieve and reset encoder values on-demand from the phone, though such utilities should not be difficult to implement.

3.3 Modifications

Some hardware modifications have been made to the robot. Upon the uptake of this project, AntBot was powered by six 1.2V AA NiMH batteries wired in series (using a simple power pack). This power pack was connected to the motor board (and subsequently the motors) by a pair of 9V connectors. The robot had to be partially deconstructed to connect or disconnect the batteries from the motors. The batteries themselves had to be extracted from the power pack and charged individually. These actions, repeated often by the current project and predecessors had caused wear on the

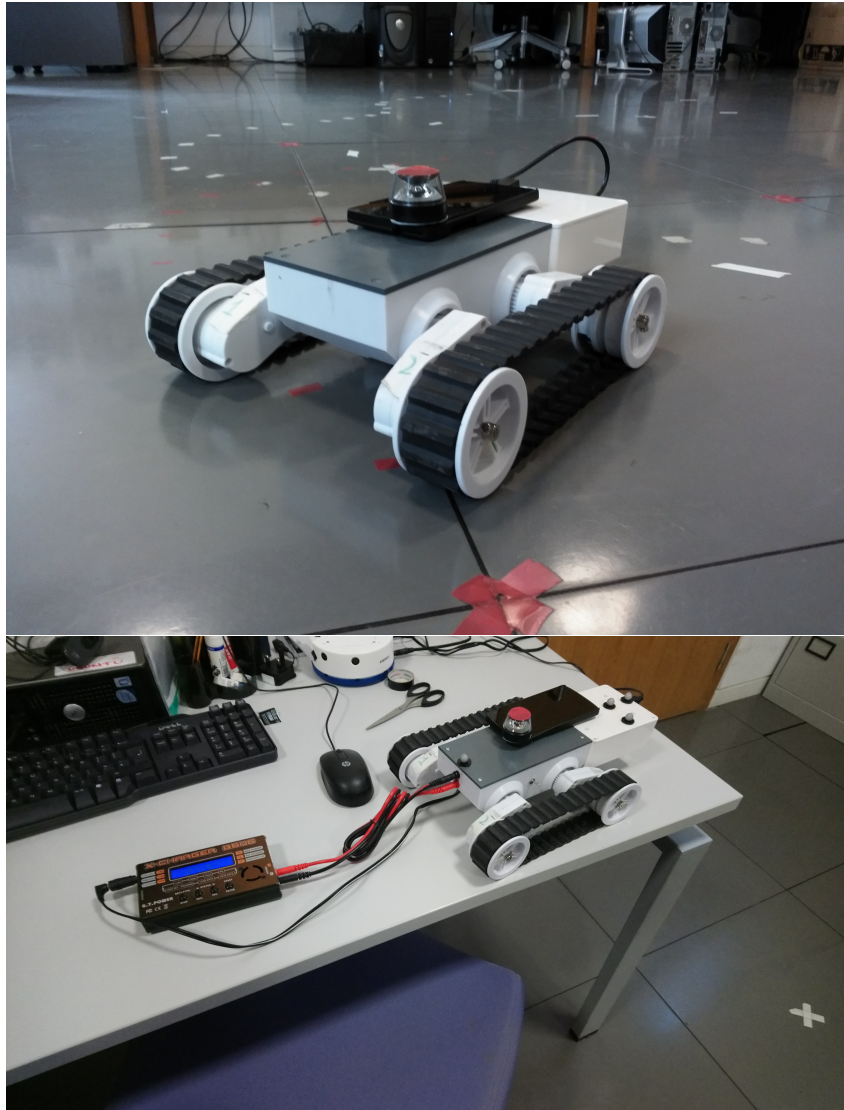


Figure 8: AntBot pre (top) and post (bottom) hardware upgrade. We can now charge AntBot directly. Note the addition of motion capture tracking markers for the Vicon system.

power pack and the internal wiring. The connections needed re-soldered multiple times. In order to have a more robust platform for testing, the on-board power system was modified. A new power source which could be charged as required without removal was added, along with external charging ports and a switch. The internal wiring was set up such that power could either flow from the external ports to the battery, or from the battery to the motors controlled by the external switch. The new power source is a 9.6V NiMH power pack. Motor speeds and systems dependent on them required re-tuning after completion of the modifications. The required modifications to chassis (holes drilled for components) were done by the Informatics workshop. The wiring, research and sourcing of parts were performed as part of this project.

4 Methods

4.1 Optical flow models for Collision Avoidance

4.1.1 Time-to-Collision

We attempted to follow the outline presented by *Low and Wyeth* as, at first glance, it seems a straightforward and neat solution. However, this method of computation for the TTC relies on the assumption that the camera view only ever moves in the forward direction [9] which is not appropriate for AntBot (see Section 3). So instead, we look at the paper by *Souhila and Karim* for an alternative; for this method, we must compute the *focus of expansion* or FOE, however, their method of estimating the FOE and did not translate well into AntBot giving a wildly fluctuating FOE. A more general method for computing the FOE is given by *O'Donovan*[10]:

$$FOE = (A^T A)^{-1} A^T \mathbf{b} \quad (4)$$

$$A = \begin{bmatrix} a_{00} & a_{01} \\ \dots & \dots \\ a_{n0} & a_{n1} \end{bmatrix} \quad \mathbf{b} = \begin{bmatrix} b_0 \\ \dots \\ b_n \end{bmatrix}$$

Where, for each pixel $p_i = (x, y)$, the associated flow vector is given by $\mathbf{v} = (u, v)$. We then set $a_{i0} = u, a_{i1} = v$ and finally $b_i = xv - yu$. The TTC can then be computed as:

$$TTC = \frac{r}{v} = \frac{y}{\frac{\partial y}{\partial t}} \quad (5)$$

Where y is the vertical distance of some point $p = (x, y, z)$ from the FOE, $\frac{\partial y}{\partial t}$ is the velocity of translational motion of y , and r and v are as given in Equation (1). A full derivation is given by *O'Donovan* from whom we have adapted this equation.

Finally, we can simplify this to the desired equation from [12]:

$$TTC = \frac{\Delta_i}{|\vec{V}_t|} \dots \quad (6)$$

Where Δ_i is the distance of a point $p_i = (x, y)$ from the FOE, and $|\vec{V}_t|$ is the translational velocity of the camera computed from optical flow²[12].

The time-to-contact is computed on a subset of pixels to the front of the robot. This time-to-contact is then appropriately thresholded and a reaction is generated based on the position of the focus of expansion which provided a simple method of replicating the balance strategy used by [12] as the FOE will be drawn to one side based on the motion parallax observed. Initial instability in the computation of these properties was countered with by averaging the properties across a series of frames to reduce potential noise.

²We must note that *Souhila and Karim* are not specific as to how they compute the camera velocity, in context it seems that they use optical flow techniques, however, their robot is equipped with wheel encoders.

The generated responses were to be halt on detection (for debugging purposes), and triggering of a smooth turn away from the obstacle. This technique was designed to be used with a sparse optic flow field, however, a version using a dense flow field was attempted. The computation across a dense flow field was found to be impractical. No formal results have been collected using this system; any apparent functionality was found to be luck instead of a working system. Analysis of functionality of such a system on AntBot is left for Section 6. The use of depth information, as in [9, 12], was planned, but as the TTC is pre-requisite for computing image depth the system never reached that stage.

4.1.2 Filtering

Here a dense optical flow field is used, and in order to explain the filtering process, it is important to discuss the flow computation itself. The optical flow is computed using openCV’s *calcOpticalFlowFarneback()* function. When given two consecutive frames the function returns a matrix M of arrays of type double. $M_{y,x}$ is a one-dimensional array of length two which contains the displacement in each axis of the respective pixel (i.e. $M_{y,x}[0]$ gives the displacement of the x coordinate, and $M_{y,x}[1]$ gives the displacement of the y coordinate).

An optical flow filter was previously implemented by *Scimeca* for the purpose of speed retrieval (Figure 9). This filter represents the expected motion observed when the robot moves forward through a clear environment. Thus, if an obstacle is present, motion parallax will cause one side to appear to move faster than the other. So collision avoidance relies on detecting a significant difference in motion between two sides of a flow field. With this in mind, we repurpose the flow filter from [11]. Though inspired by [13], our method for performing the computation and avoidance was modified for the sake of implementation on AntBot, instead mirroring *Scimeca*’s method of speed retrieval.

Instead of creating a left and right filter, we create left and right flow frames by rotating the image frame by a certain angle left or right as in [11]. However, we reduce the angle from $\pm 45^\circ$ [11] to $\pm 16^\circ$. It was found that the size of this angle had a mild effect on the region of the image which would trigger responses; a larger angle would result in higher sensitivity to the sides of the robot, a smaller angle results in lower side sensitivity which was desired for the CA system. We only want the robot to avoid obstacles to the front, obstacles to the sides should not trigger responses. The offset angle was tuned manually and $\pm 16^\circ$ was found to perform well; smaller angles resulted in an insensitive system, and larger resulted in more noise though performance was still good. The filter itself is second filter from [11] which was already implemented on the robot.

The filter is constructed as an $N \times 3$ matrix F such that:

$$F_i = \begin{bmatrix} \sin(-\pi + i \frac{2\pi}{N}) & 0 & 0 \end{bmatrix} \quad \text{for } i \in \{0, N - 1\} \quad (7)$$

where F_i is the i th row of F . Intuitively each row corresponds to a pixel value in the x axis.

Once the filter is computed, we retrieve the flow for each pixel by adding the displacements retrieved from *calcOpticalFlowFarneback()* to the pixel value. For each

value of x we also apply an offset of $\pm 4px$ which corresponds to our left and right frames centred at $\pm 16^\circ$. We can summarise the filtering process as:

Let M be the matrix returned by `calcOpticalFlowFarneback()`.

For each x, y we will:

Compute pixel's starting location in the shifted frames as:

$$\begin{aligned} PLF &= [\quad (x + 4) \pmod{N} \quad y \quad] \\ PRF &= [\quad (x - 4) \pmod{N} \quad y \quad] \end{aligned}$$

Compute the flow vector from the start location to where it is now as:

$$\begin{aligned} CLF &= [(M_{y,x}[0] + x + 4) \pmod{N} \quad (M_{y,x}[1] + y) \pmod{R}] \\ CRF &= [(M_{y,x}[0] + x - 4) \pmod{N} \quad (M_{y,x}[1] + y) \pmod{R}] \end{aligned}$$

Extract the correct filter vector from matrix F (Eq. 7):

$$\begin{aligned} LFilter &= F_{PLF[0]} \\ RFilter &= F_{PRF[0]} \end{aligned}$$

Apply the filter:

$$LFD = LFilter \cdot CLF \tag{8}$$

$$RFD = RFilter \cdot CRF \tag{9}$$

Where N is the number of horizontal pixels and R is the number of vertical pixels. Here we have $N = 90$ and $R = 10$. Now LFD and RFD represent how much the observed flow deviates from the expected flow for a given pixel on the left and right respectively. We then sum this over the shifted image frames to get the total difference between expected and observed flow:

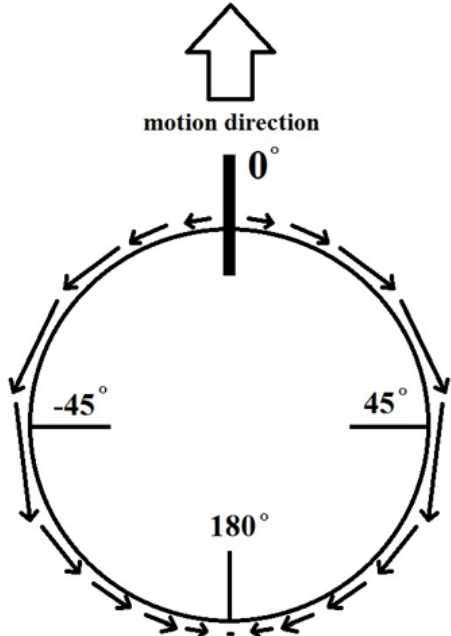
$$LeftFlowSum = \sum_{i=0}^{K-1} LFD_i \quad RightFlowSum = \sum_{i=0}^{K-1} RFD_i \tag{10}$$

Where $K = N \cdot R$, and LFD_i is the LFD value computed for the i th pixel. Now we have defined a way of computing the observed speed on either side, we can start to define behaviour. In the case an obstacle is seen on one side of the image, we expect the speed on that side to be higher due to motion parallax. Thus, we simply compute the difference between the two sums:

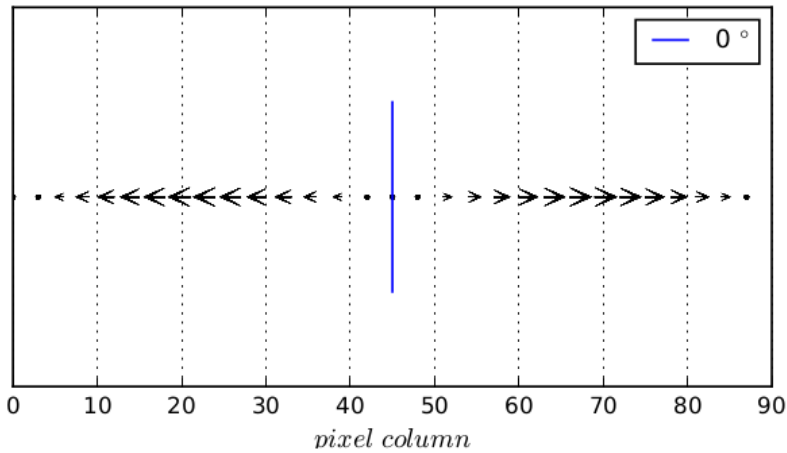
$$FlowDifference = LeftFlowSum - RightFlowSum \tag{11}$$

which gives us our final stimulus to be used to generate a reaction. Large positive $FlowDifference$ means we have seen an obstacle on the left, similarly, large negative $FlowDifference$ means we have seen an obstacle on the right. Here we employ the idea of “leaky” accumulators from [13]. An accumulator is kept for both sides of the frame. The difference is thresholded to account for noise such that only significantly positive or negative values contribute to behaviour; this is known as the *accumulation threshold*. Once the accumulator on one side exceeds its *reaction threshold*, an immediate turn away from the perceived obstacle will be performed. The turn is simply

a $\pm 20^\circ$ rotation using the robot's *turnAround()* function. The accumulators are reset periodically to avoid a build up of old flow information. A separate method of accumulation was trialled out of interest whereby a single accumulator would be fed the raw (thresholded) difference and a sufficiently large positive or negative value would trigger the appropriate response. No difference was noticed in performance and so separate accumulators were kept. While this implementation was simple, and not as refined as we would have liked, it did demonstrate impressive performance in navigating arenas of varying obstacle density.



(a) Motion pattern



(b) Implemented filter(s)' response

Figure 9: The filter implemented by *Scimeca*: (Caption by *Scimeca*, Figure 13): Figure (a) shows the idea behind the modification of the filter for speed retrieval. When moving forward, for example, we expect the rectangular 360 [degree] image to have vector flows in different length throughout the frame, in the pattern shown in the Figure.

Figure (b) shows the filter response of the modified filtering process for this [*Scimeca's*] project. During matching, the found flow vectors will be projected onto the corresponding filter vectors nullifying the information on the y axis and scaling the vectors differently depending on the area of the image they are found in.

4.2 The Mushroom Body

This section will be less of a formal declaration of method, and more a discussion of the process undertaken to get the Mushroom Body circuit working in a robust manner (see Section 2.3).

The Mushroom Body circuit (implemented as a Willshaw Net) was originally implemented by *Eberding* when he developed the platform. Though the implementation does mirror the model of *Ardin et al.*, the model struggled to perform to the same degree despite potentially having more visual information due to the higher resolution image of AntBot. The nature of our experimental scenario required (at least initially) that a scanning behaviour be used to perform visual navigation and this is the context in which we shall frame our discussion; *Zhang* did manage to achieve significantly improved results using klinokinesis as a route following strategy. Initial attempts at scanning resulted in extremely poor performance with seemingly no capacity for memory present in the network beyond blind luck. The first and most obvious issue was the scanning behaviour itself; while the robot was to turn through a 60° arc in increments of 6° , the actual arc was far larger ($> 100^\circ$). On closer inspection of the control code on the Arduino, the problem could be seen as the control method. The turning command relies on a calculation based on encoder clicks per degree; while simple and appropriate for general use, this style of control generally struggles to make precise movements, such as scanning increments.

To remedy this, we opt for a different style of scanning which we will refer to as *visual scanning*. Since AntBot has a 360° view, we instead take a still image, and rotate it, showing each rotated frame to the network and receiving a familiarity measure; this change was felt justified as we are concerned with the performance of the MB model and did not wish to be hampered by robot control issues (though these issues can, and we feel should be fixed if possible - see Section 7). These values are stored in an array (as with standard scanning), the minimum value is selected and the angle computed by taking the distance from the centre-point of the array and multiplying by the number of pixels traversed horizontally then multiplying again by the constant 4 (degrees/pixel). In the first iteration, a fine grained scan was used, however, this was found to be less effective and more prone to erroneous familiarity measures. Reducing the number of image angles while scanning over the same arc resulted in more stable performance. In total 17 different angles (from $-16px$ to $+16px$ in increments of $2px$) are compared. The image rotation itself is done with a basic array rotation algorithm which manipulates matrix columns. With the visual scanning, the problem of robot control was largely eliminated.

However, a common behaviour was still observed. Be it physical or visual scanning, the robot always performed a turn in the same direction, at the same angle (i.e. the most familiar direction was always to the extreme left). For the purposes of debugging and visualising the network and its outputs a two-part tool *AntBotStats* was developed (see Section 4.3). Visualising the output of the network showed that the returned familiarity was not following the correct pattern over a scan.

In figures 10 and 11 (both produced using visual scanning) we see that the pattern being returned by the early network with scanning was far from what it should have been. The EN response of 0 should, in theory, correspond to the most familiar angle. Figure 10 clearly shows that there is a problem with the Kenyon Cell activation in the

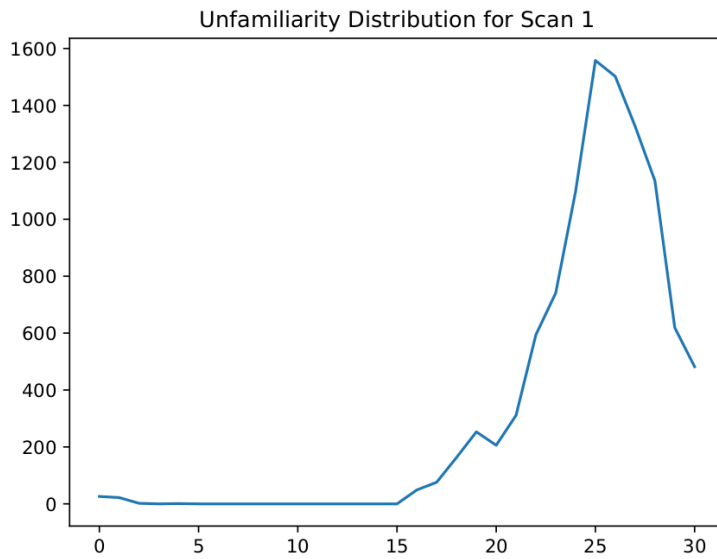


Figure 10: The erroneous familiarity pattern displayed by the network. The plot shows the familiarity response of the Extrinsic Neuron (y-axis) against the index of the scan (x-axis). 0 denotes the leftmost direction, 15 directly ahead, and 30 the rightmost direction. This was a simple plot produced early in the debugging process, hence the lack of axis labelling and higher number of scan points.

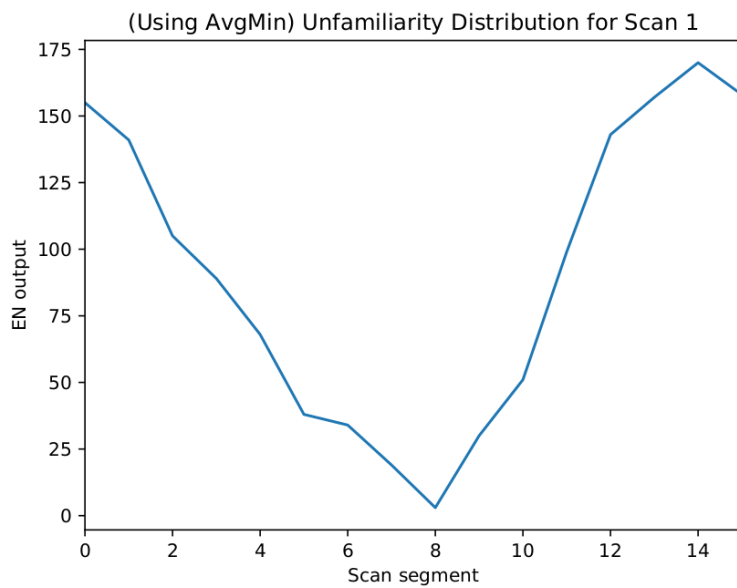


Figure 11: The expected familiarity response of the Extrinsic Neuron. Note the improved range of the response along with the clearly defined minimum.

network; a presented image should activate somewhere in the range of 200 to 500 KCs (this is rough due to the pseudo random construction of the network). The EN response shows that at least 1500 KCs were activated by some scan angles; in almost all cases, an EN response of 0 was caused by a lack of any KC activation or sufficiently low KC activation (the unfamiliarity measure was initialised as 0 in the network). To, fix this upper and lower thresholds on KC activation were added to the network. If KC activation lay outside these bounds a *maximum unfamiliarity* measure was returned; this value was defined as the maximum number of KCs activated by an image during the learning process [17]. The justification for introducing bounds on KC activation was that too few KCs did not give enough information, while too many represented noise in the network. Regardless of the justifiability of this decision we were still experiencing KC activation problems and *Ardin et al.* did not encounter such problems in their functionally identical model.

It is here we must note again, *Zhang's* improved performance using klinokinesis; this suggests that the network itself is likely not the issue. Upon performing further debugging the problem revealed itself to be a bug in the visual scanning though we think the problem was the same as that experienced by the phsyical scanning, just introduced in a different manner. Due to a quirk of OpenCV in Java, the *Mat* (matrix) objects are subtly passed by reference, there is no syntax for this, and it is not the expected behaviour in Java. When Mat objects are passed, a separate object called the *matrix header* is actually passed which performs the same function as a pointer in a C-style language. Thus, the image rotation algorithm was working correctly, but the image was being rotated in unexpected ways as we were treating this as a pass-by-value scenario. Simply, creating a copy of the Mat object inside the rotation function fixed the issue and the system began functioning correctly. Final tuning of the brightness threshold for KC activation was then performed.

The final model is largely the same as in [6]; the only real modification being the Kenyon Cell thresholding. Normalisation of the PN input was implemented but not found to make a noticeable difference in terms of KC activation so raw PN values were used to reduce complexity in the model. Normalised PNs may be included in future iterations. While KC activation thresholding should not strictly be necessary, it was kept as a safety mechanism in the final model.

4.2.1 Real Weightings

An alternate version of the Mushroom Body circuit was constructed using real-valued weights as opposed to binary ones. This version was adapted from the existing model, changing only the construction of the KC weight matrix and the weight decay procedure. In this version, each KC starts with a weight of 1. KC activation remains the same, however, on activation we take the weight and multiply it by some learning rate α (the initial model has $\alpha = 0.9$). This weight decay occurs on every activation of the Kenyon Cell. The idea is a standard one in machine learning; the more the network observes a pattern, the more familiar that pattern becomes. The motivation for such a model is simply to remove the instantaneous learning aspect of the original model. In reality, learning and memory are not two distinct processes. Recalling can help reinforce learning. As an example, we could allow AntBot to learn continuously throughout the homeward experiment presented in Section 6; we would hope to see the routes become more accurate over each run. Though this model was not used during this project, it

was developed as a prototype and felt worth discussing briefly.

4.3 AntBotStats

To aid in debugging the Visual Navigation system and production of results a two-part tool, *AntBotStats* was developed. The tool consists of an on-board Java class, *StatFileUtils* (adapted from *LogToFileUtils* [17]) and a Python parsing and plotting tool. The *StatFileUtils* class is designed in such a way that title, plot type, and data can be specified. The Python system then reads the file, produces the correct plots and outputs them to a PDF for viewing as a collection. The tool is currently quite basic but is designed to be easily extensible to produce different information; for example a module was added to produce trajectory plots from the Vicon motion capture system. We would like to develop this tool further so that a more polished version can be made available to future students.

5 Experimentation

5.1 General

An experimental arena was constructed on the old Robocup practice pitch in G.17 in the Informatics Forum. This space was chosen for its suitable size, locality, and easy access to recording equipment for Visual Navigation experiments. An enclosure was constructed using old (mostly) preconstructed perimeter sections from the Robocup pitch which could be easily set up and dismantled as the space was shared. The enclosure was added to act as a visual blind (Figure 12) in an attempt to reduce the background noise observed by the robot and also to keep the distances on either side reasonable as it was noted by [11] (and experienced first hand) that large differences in distance on either side of the robot could cause drastic differences in the speed observed by the optical flow which would affect our experiments. The perimeter blind was aligned with the tape markings of the football pitch to establish consistency.

As obstacles, early tests involved the use of large, obvious objects such as cardboard boxes. To try and create a more realistic picture for AntBot, simple synthetic tussocks were constructed. These were constructed by taking $1m^2$ synthetic hedge wall panels and cutting them down to different sizes. These were then glued to rough-cut (in an effort to keep sizes non-uniform and somewhat natural) wood blocks. The wood blocks compensate for the distance from the ground to AntBot's view height such that AntBot can only see the synthetic plant (Figure 13).

5.2 Collision Avoidance

Collision avoidance experiments aimed to test the basic functionality of the system; once demonstrated, we then wished to show the robustness of the system. Finally, some experiments were performed out of sheer curiosity to determine how predictable the system was and how well it coped with less random patterns of obstacles. Each of the main experiments took place in a set arena and consisted of five runs to observe the consistency in performance. Each run lasted 30 seconds as the robot could usually navigate the length of the arena in this time. For information on timing and



Figure 12: The empty experimental arena.



Figure 13: An example of the tussocks used during experiments.

synchronisation inconsistencies please see Section 7 on software engineering.

We start by demonstrating the basic functionality of the system using a series of three basic arenas: An empty arena, a single large obstacle (a cardboard box present in the lab), and finally basic tussock interaction to ensure that the robot could detect and react to the synthetic tussocks.



Figure 14: The arena used for basic tussock interaction

Once basic functionality is established, we then partition the arena into quadrants and start to increase tussock density per quadrant. Starting with a density of $1/\text{quadrant}$ the tussocks were placed randomly, as density increased tussocks were placed more deliberately to attempt to block paths the robot had used previously (while still permitting enough space for the robot to navigate through the environment). The arenas can be seen in Figures 15, 16, and 17. For these experiments in increasing complexity, the robot was always started from the South West corner of the arena so that, regardless of the arena set up, the robot would have to perform some collision avoidance movements. The reader should note that the initial tussock in the South East corner was a little more limited in where it could be placed. If placed too far to the North, the avoidance turn triggered would turn the robot away from the arena; while this is technically successful as the robot avoided the obstacle, the run would provide no

useful data as the robot had not attempted to navigate the more complex arena; thus the tussock in question was placed in a location that would trigger an inward turn. Each run was assessed on three criteria: Number of collisions, Number of failed avoids, and whether or not there was a *risk-on-end*. A collision was a direct impact with an obstacle that should have been avoided where no turn was triggered in response (or the turn only occurred well after the collision). A failed avoid occurred in the case where the robot did react but it was too late in doing so, or the robot could not turn enough due to space constraints. The risk-on-end occurs when the robot is about to have a collision and the timer runs out (i.e. a collision would have occurred in any other navigational scenario); these occurred frequently, however, the vast majority of them would involve a collision with the side of the arena.

The final series of tests for the CA system involved setting up pre-determined arenas to see if the robot would respond in a predictable fashion when presented with a particular pattern of obstacles. Some arenas were designed to test tuning parameters on the robot, for example, to test how speed of the robot affects the reaction time and sensitivity of the system. These experiments presented largely unexpected though useful and thought-provoking results.



Figure 15: Arena 4. One tussock per quadrant.

5.3 Visual Navigation

Visual navigation experiments were again conducted across different arenas. These arenas were designed in such a way that the optical flow would have little difficulty navigating them, while still providing enough visual information as to make the images captured meaningful. A major failure in the collision avoidance system would result in a full reset (though minor failures were permitted to continue). Each arena hosted two runs, one starting from the South West corner of the arena, the second starting from the South end in the centre of the arena. A learning run was conducted using only the collision avoidance system to navigate through the arena for 30 seconds. Image learning was not performed at any set intervals; a reward signal was sent once per main loop iteration *if* the new frame was available from pre-processing (synchronisation between threads means this may not always be the case). Upon finishing the learning run, the robot was placed at the start point for the run.



Figure 16: Arena 5. Two tussocks per quadrant.



Figure 17: Arena 6. Three tussocks per quadrant.

The robot then attempts to recall the route using only visual memory. Scans were performed at regular time intervals, or if the robot encountered an obstacle during a routine forward motion. The memory run had a time limit of 60 seconds, the extra time to allow for scanning and decision making. If the robot reached the end of the route (or close proximity to the end of the route) before the time was up it would behave unpredictably as one might expect.

Eighteen experiments were run in total; the first eight were run as described above, the robot's behaviour was modified slightly for the remaining ten. For the last experiments, the reward signal frequency was increased in an attempt to gain more information about a route; in the first bout of tests, the reward signal was being sent approximately seven times per run, in the second bout this was tripled, however, some stored images may overlap. The CA behaviour was also modified to allow the robot to stop before turning instead of performing an immediate turn.

Experiments were coded as *bout-arena-run*; where *bout* could be AB or MAB for AntBot or Modified-AntBot. As an example: MAB-3-2 refers to Modified-AntBot, Arena 3, Run 2. This convention may be somewhat confusing as arenas were *not* the

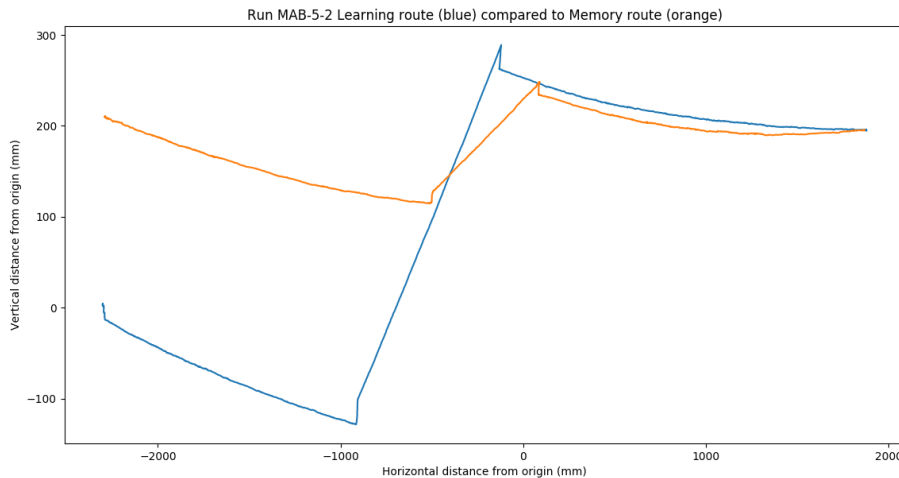


Figure 18: The autoscaled plot for run MAB-5-2.

same between bouts; MAB-3-2 and AB-3-2 did not take place in the same arena. The arena numbering was reset after modifying AntBot’s behaviour. There were four arenas for AB experiments and five for MAB experiments.

The routes were captured using the Vicon motion capture system; separate recordings were taken for learning and memory runs, the files exported in .csv format then parsed and plotted using a module in *AntBotStats*. All plots were set to the same scale so as to allow direct comparison between results without needing to account for scale. Figures 18 and 19 suitably demonstrate this; though experiment MAB-5-2 was a success, the plot shown in Figure 18 does not make this clear.

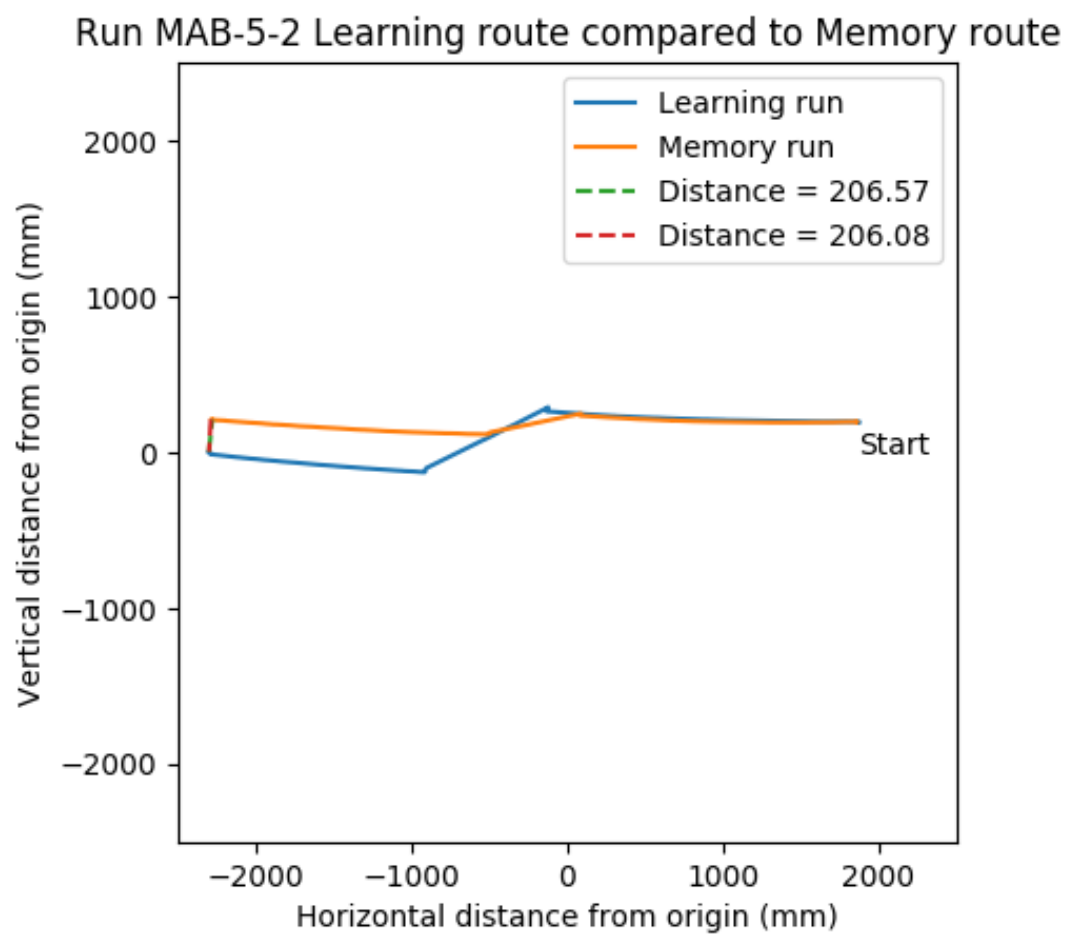


Figure 19: The set-scale plot for run MAB-5-2; forcing the axes to a uniform scale over all runs gives a more accurate immediate view of the runs and their similarity.

6 Results and Evaluation

6.1 Collision Avoidance

6.1.1 Time-to-Collision

The TTC system was implemented with both flow field types; quite simply, performing the computation on a dense flow field resulted in drastic reduction on speed and accuracy. We will discuss in the context of a sparse flow field. The sparse optic flow field is computed using the *Lucas-Kanade* method on the points returned by OpenCV's *goodFeaturesToTrack()* function. This function returns a Mat object which indicates the strong corners in an image. In essence, it locates prominent features in the image which can provide consistent information. Inconsistencies were noticed in the computation of the FOE and the speed (and hence the TTC) and many *dirty* fixes were required to get the computation functional. For a straightforward matrix calculation, this should not be the case. As the entire method was dependent on the output of *goodFeaturesToTrack()*, we felt it appropriate to check that the values being returned here were in-fact reliable. The flow vectors detected using the points returned by *goodFeaturesToTrack()* can be seen in Figure 20. Though the changes are not drastic, it can be seen firstly that varying motion is being detected in the image where none exists though this *noise* can be expected somewhat. Secondly, it should be noted that the different frames show different numbers of features. While sat still, the algorithm cannot reliably detect consistent corners in the image. While the slight differences in flow are not of major consequence, the different feature count was found to have a large effect on the consistency of the computation as, every other frame, we are considering new information, and perhaps missing information we had previously.

This flow information is key to computing both the speed of motion and the focus of expansion of the flow field; thus, the time-to-contact is not accurate nor consistent. Though TTC was abandoned as a method for collision avoidance as part of this project, there are a number of modifications that could be applied to make this more stable, however, any method of computing the TTC relies on an accurate speed calculation. The works on which we based this system have access to far more reliable speed information through the use of encoders or flow computed with a high definition camera. The speed information available from AntBot's optical flow speed retrieval

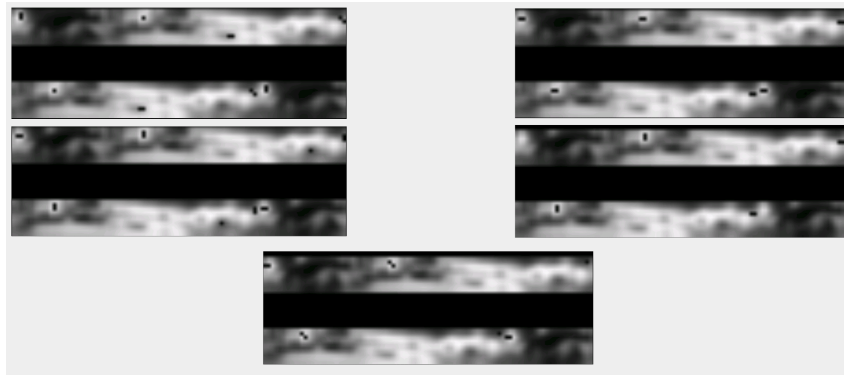


Figure 20: $\pm 45^\circ$ offset image frames showing the flow vectors computed at each point (distinct black pixels). The five images were taken over the course of one minute while the robot was stationary in G.17.

Optical Flow Functional Performance						
	Arena 1	Empty		Arena 2	Single Box	
Run	Collision	Failed avoid	Risk on end	Collision	Failed avoid	Risk on end
1	0	0	Yes	1	0	Yes
2	1	0	Yes	0	0	No
3	0	0	No	0	1	No
4	0	0	No	0	1	No
5	0	0	No	0	0	No
Arena 3		Tussock Interaction		Arena 4	1 per quad	
Run	Collision	Failed avoid	Risk on end	Collision	Failed avoid	Risk on end
1	0	0	No	0	0	No
2	0	0	No	0	0	No
3	0	0	No	0	0	No
4	0	0	No	0	0	No
5	0	0	No	0	0	No
Arena 5		2 per quad		Arena 6	3 per quad	
Run	Collision	Failed avoid	Risk on end	Collision	Failed avoid	Risk on end
1	0	0	Yes(*)	0	1	No
2	0	0	No	1	0	Removed(**)
3	0	1	No	0	0	No
4	0	1	No	0	0	Yes
5	0	1	Yes	1	0	No

Table 2: The results for the functional performance experiments on the filtering CA system.

(*) This was the only case of a risk on end coming from a tussock during formal experiments, all other potential collisions were with the side of the arena. (**) The first turn the robot made took it away from the arena in the manner described in 5, the collision was with the arena wall in the South East corner as the robot had no where left to go.

system is less accurate, though we could implement an encoder based system while remaining biologically plausible [16]

This CA system was abandoned and the reader should note that the code is still on the robot, though commented and with a great amount of functionality removed. The menu option on the robot was repurposed to allow easy debugging of other procedures in the last stage of the project. In short, no functional implementation is on the robot at this time, though the remnants of the implementation are still present.

6.1.2 Filtering

The filtering system proved to be quite robust in its operation; over the thirty functional performance runs we only note four direct collisions (complete failures of the system), and six partial collisions (the robot corrected but did so too late, or knocked a tussock on the way past). The full set of results for the functional performance experiments are shown in Table 2.

Collisions were often the result of avoidance turns putting the robot on a collision course with another tussock (even when there was perhaps a clear path had the robot turned the other way). We drew no distinction between collisions with tussocks and

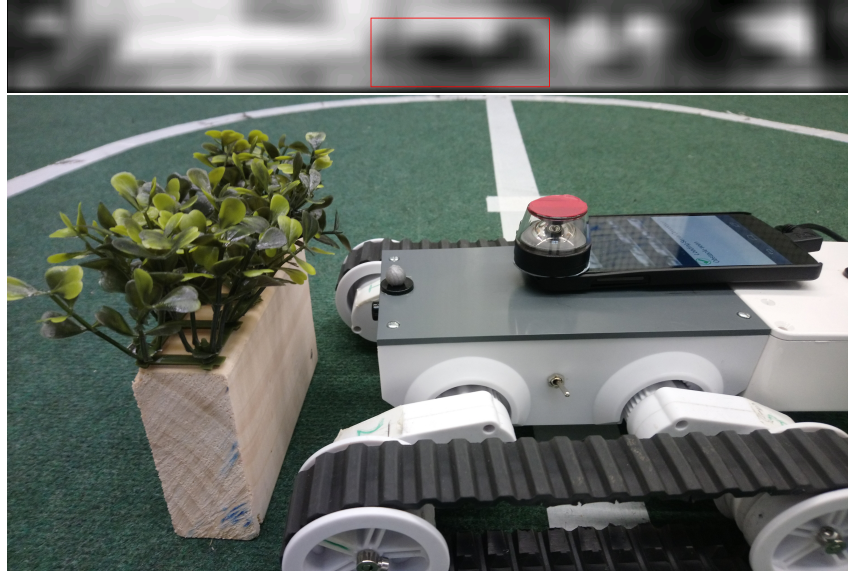


Figure 21: The appearance of the tussock in the visual frame (boxed in red). Though the tussock is completely obstructing the frontal section of the robot’s view, the tussock is comparatively small in the visual frame. This image was taken without the enclosure.

collisions with the arena wall hence, the single collision in the empty arena; this collision is an interesting one as there is seemingly no reason for it to occur. Why is it that the AntBot reacts when there is no obstacle and when flow discrepancies should be minimal (due to the white boundary)? One may also ask why the AntBot would, in avoiding one obstacle, turn toward another. Both questions result in the same conclusions (which will be reflected in the results of more rigid test scenarios to follow). Firstly, while the system performed well, the detection and response system is quite crude. A smooth arc would be a much more desireable behaviour for responding to flow stimuli, and indeed, this was the behaviour in the first iteration of this system; it was removed as the number of failed avoid maneuvers was much greater due to the robot’s inability to perform such movements quickly. Even more desireable would be a proportional feedback control system, however this presents a number of technical challenges for the AntBot. Secondly, AntBot’s view is rather distorted due to the 360° lens attachment. The high-wall enclosure was introduced to reduce the effects of background noise however, AntBot can actually see out of this arena. The lens distortion also presents challenges with the tussocks. While they are visible, they are extremely small in the image frame unless placed directly in front of the robot (Figure 21). The simple solution would be to construct larger tussocks. The area observable outside the arena will have minimal effect unless there is no immediate stimulus in the arena, however it may cause problems if the stimulus is out of range (i.e. not yet effectively visible to the camera).

Figures 22, 23, and 24 show the three arenas used for behavioural experiments. These experiments helped to highlight the issues mentioned following the functional results. In each case, the desired behaviour is fairly clear from the layout of the arena: In the diagonal case, we want the robot to turn right and either follow the wall or move away from it, in the curved case we want the robot to follow the curve or turn away from it completely, and finally in the fluted case, we want the robot to move straight through the opening between the two walls. In all but one experiment in Arena 7, the robot

Optical Flow Behavioural Results						
	Arena 7	Diagonal wall		Arena 8	Curved wall	
Run	Collision	Failed avoid	As expected	Collision	Failed avoid	As expected
1	1	0	No	1	0	Almost
2	1	0	No	1	0	Almost
3	1	1	No	0	0	Yes
4	1	1	No	1	0	Almost
5	1	0	Almost	1	0	No
Arena 9						
Run	Collision	Failed avoid	As expected			
1	1	0	No			
2	1	0	No			
3	1	0	No			
4	1	0	No			
5	1	0	No			

Table 3: The results for the behavioural experiments conducted on the optical flow system; for these, arenas were designed to elicit a certain behavioural response, however, they mostly failed to do so, highlighting problems with the current implementation and methods of experimentation. The “As expected” column denotes cases whether the robot performed the expected moves: No means not at all, Almost means that movements were initially correct then went wrong, and Yes means complete success.



Figure 22: Arena 7. The diagonal wall arena.



Figure 23: Arena 8. The curved wall arena.



Figure 24: Arena 9. The fluted walls arena.

reacted early, turning towards the wall instead of away from it. We think this is because of the visual distortion; visual noise from outside the arena is more prominent than the tussocks and thus causing an unnecessary reaction. Placing the robot further West (closer to the first tussock) generated the desired response. In three of five runs in Arena 8, the robot reacted correctly initially, but in moving away from the wall of tussocks it would lose sight of it and ultimately turn back towards it resulting in a collision; one run was a complete failure. Again, the robot may be reacting to the visible area outside the arena once the tussocks become too small in its field of view. In all cases in Arena 9, the robot reacted to one side of the flute (despite the fact it actually had a clear path) and run into the opposite side. Making the flute wider allowed to robot to behave as desired so there is either not enough detail in the image, or the gap appears too small to AntBot, and thus it thinks there is no route open to it.

These three simple tests back up the points raised earlier. In both Arena 7 and 9 the robot is reacting to situations where no reaction is necessary. Again, this points to the effect of noise in the flow frame though, we may also question the choice of filter. The filter was chosen for simplicity as it was already on-board and had demonstrated the capacity to compute fairly accurate speed information [11] with a dense flow field; though usage of the existing filter was justified, it may be worth considering something different. While we feel good results were achieved, it is apparent that many refinements can, and indeed should be made (see Section 7).

6.2 Visual Navigation using the Mushroom Body

Results: The results for the Visual Navigation portion of the project are harder to quantify. It is clear that the Mushroom Body circuit demonstrates the capability to perform robust route navigation through a somewhat cluttered environment. Though rare there were cases where the robot would lose the route and regain it again through drastic self-correction; there are some cases where the correction could be deemed luck, and in others the correction appears more genuine. Here we present some of the more interesting plots for discussion along with a table summarising our results. The complete set of plots is available in Appendix A.

An example plot can be seen in Figure 25. The blue route marks the learning run performed using Collision Avoidance. The orange path marks the route the robot then recalls from memory. The start point is clearly marked. We also take two distance measures (taken in *millimetres*) which are marked on the plot for convenience. The first distance measure (green dashes) is taken from the final point in the learning run, to the closest point, using euclidean distance, on the remembered route. The second distance measure (red dashes) is taken from the final point in the memory run, to the closest point in the learning run. We include both distance measurements due to the effects of inconsistent timing in the experiments (see Section 7).

In certain cases, one distance measure provides more useful information than the other. Often, the memory run would be physically longer than the learning run, occasionally they were the same length, and even more occasionally the memory run was shorter. Once the robot reaches a location near the end of the learning route, visual information becomes less meaningful. There is no feedback to tell the robot to stop. So we take the nearest point on the memory run to the end of the learning run as the robot has gone as far as it reasonably can using visual memories. Should the memory task run out of time

before it can reach a point near the end of the learned route this distance measure becomes meaningless, as we have no way of knowing how the robot would have gone on to behave. Instead, we then take the distance from the end of the memory route to the closest learned point, giving us a measure of how far we were from the route on stopping, and what chance was had of success. Thus, we measure both distances take the most useful measurement, though this may not always be the one that points to success.

Due to the size of the AntBot and the arena, the error threshold of $> 20\text{cm}$ used by Ardin *et al.* is no longer a good measure of error. A variance of 20cm was actually seen as very good in terms of accuracy at this scale. If we expand our error to be 65cm then we get a far better threshold. As can be seen from the collection of plots in Appendix A, the robot has a good chance of recovering its route when it is approximately 65cm off course. Further than this, and the robot will likely only recover by luck. There are cases however, where common sense must come into play. Take for example, Figure 28. In the case of AB-1-2 we might be tempted to take the shorter red distance as our final error. The memory run appears (slightly) shorter, and this could be counted as a success by our interpretation, however, in this case we cannot give the model the benefit of the doubt. It is clear from the figure that the robot would not have recovered the route so we count this as a failure. Unlike previous experiments which used the MB circuit, the agent was not corrected in the case of error. We instead allowed it to complete the run to see how it would behave (i.e. when the agent loses the route, does its behaviour match that of the ant). Successes and failures were judged on the success of the navigational task alone; we did not consider behavioural accuracy. Summary results are presented in Table 4.

Visual Navigation Summary Results				
Run	Green distance (mm)	Red distance (mm)	Distance taken	Success
AB-1-1	419.14	413.35	N/A	Yes
AB-1-2	1346.24	473.58	N/A	No
AB-2-1	86.04	177.99	Green	Yes
AB-2-2	1494.37	619.01	Red	Yes (**)
AB-3-1	270.19	595.29	Green	Yes
AB-3-2	469.03	466.09	N/A	Yes
AB-4-1	733.95	849.13	Green	No
AB-4-2	623.86	573.33	Red	Yes
MAB-1-1	958.23	1786.78	Green	No
MAB-1-2	364.03	465.03	Green	Yes
MAB-2-1	244.56	319.14	Green	Yes
MAB-2-2	322.33	422.53	Green	Yes (*)
MAB-3-1	147.34	156.86	N/A	Yes
MAB-3-2	858.28	1047.04	Green	No
MAB-4-1	610.47	610.54	N/A	Yes (**)
MAB-4-2	131.21	130.73	N/A	Yes
MAB-5-1	428.73	100.95	Red	Yes
MAB-5-2	206.57	206.08	N/A	Yes

Table 4: The summarised results for the VN experiments. All distances are given in millimetres. The green and red distances correspond to the distances marked in green dashes and red dashes on the plots. Distance taken denotes the distance used to determine success; N/A was given in the case where neither measure was more meaningful than the other. For an explanation of interpretation, please see the results discussion for VN experiments. (*) While we consider this run a success, the memory route does deviate significantly from the learned route though it seems correction is attempted. (**) These are considered edge cases, by our interpretation they are successes, however they could also be considered failures (particularly MAB-4-1). This table was copied by hand; in the case the distances presented disagree with the distances on the plots, the plots prevail. We count a 77% success rate including edge cases, 66% excluding.

The results presented in Table 4, suggest that we have a great improvement over previous experiments which used a scanning route following strategy. However, we must be careful not to compare directly as previous experiments conducted by *Zhang* and *Eberding* corrected errors mid-run and used a different notion of error altogether. *Zhang* defined an error to be a $50cm$ deviation from the learned route. We were more generous as we found the agent could still recover past this distance. We cannot claim directly that we had fewer errors, though it seems safe to conclude we have had more success in accurately recreating routes without the need for manual correction.

Discussion: Figure 26 demonstrates the ideal behaviour wherein the robot zig-zags over the correct route, consistently correcting to keep itself on course. It is in this behaviour we see the model’s capacity to remember the visual corridor correctly. In Figure 25 we can see an example of complete failure in terms of navigation however, this figure also demonstrates the strength of the model. From Figure 25 see that the robot is unable to recover its route once it becomes lost as it cannot find the next point in the visual corridor. This successfully replicates the type of behaviour seen in ants when they lose their route[15]. This figure demonstrates why we chose to allow incorrect routes to continue though we do think that correction could prove useful (see Section 7). We can also point to Figure 27 to justify this decision. Here we can see the robot attempt a recovery and it appears to succeed, getting within $50cm$ of its goal endpoint with a correct heading. We show here that correcting errors is not always necessary, at times the agent may recover.

In Figure 29 we see the justification for modifying the agent’s behaviour. This run was considered successful, however it can be seen that the robot did not follow the route precisely, rather it followed an inside line. A potential reason was interpreted as the delay between obstacle detection and reaction during learning. After modification, we do not see a large difference, though we do generally see the robot get closer to its goal and successful routes seem more stable.

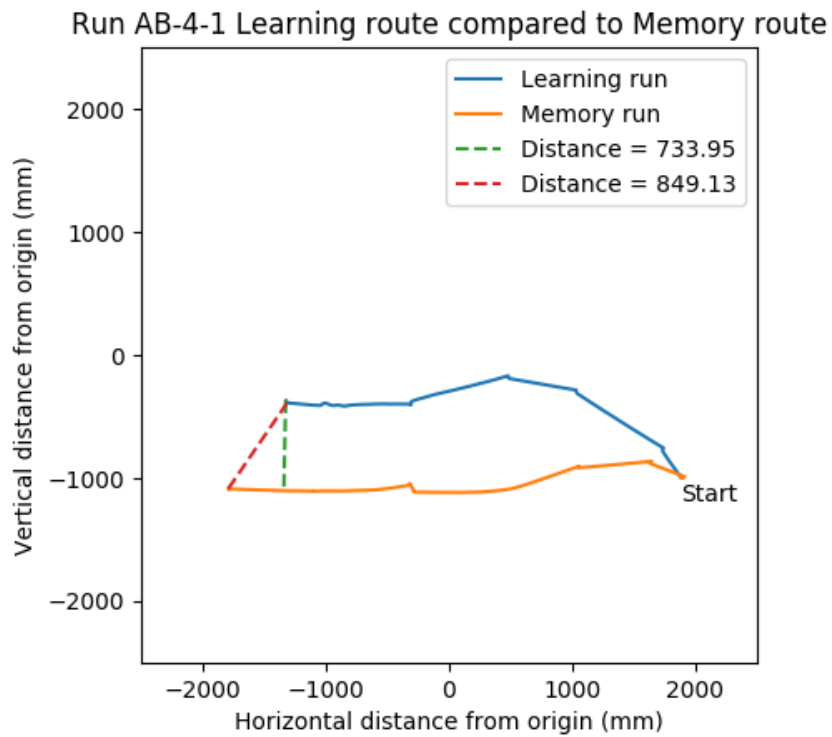


Figure 25: Trajectory plot of run AB-4-1; this run was considered a failure of the Visual Navigation system.

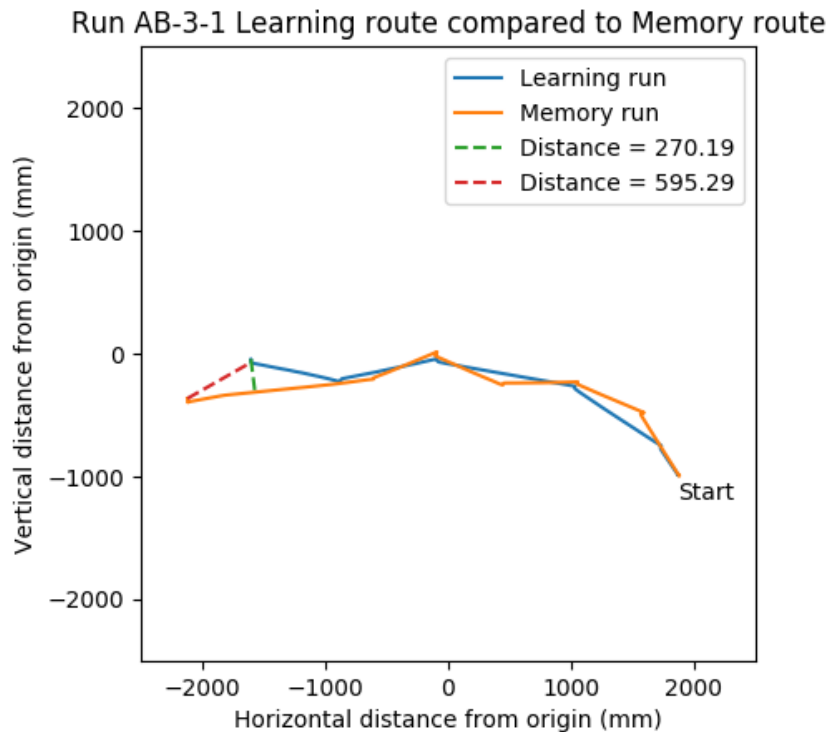


Figure 26: Trajectory plot of run AB-3-1; this run was considered a success of the Visual Navigation system.

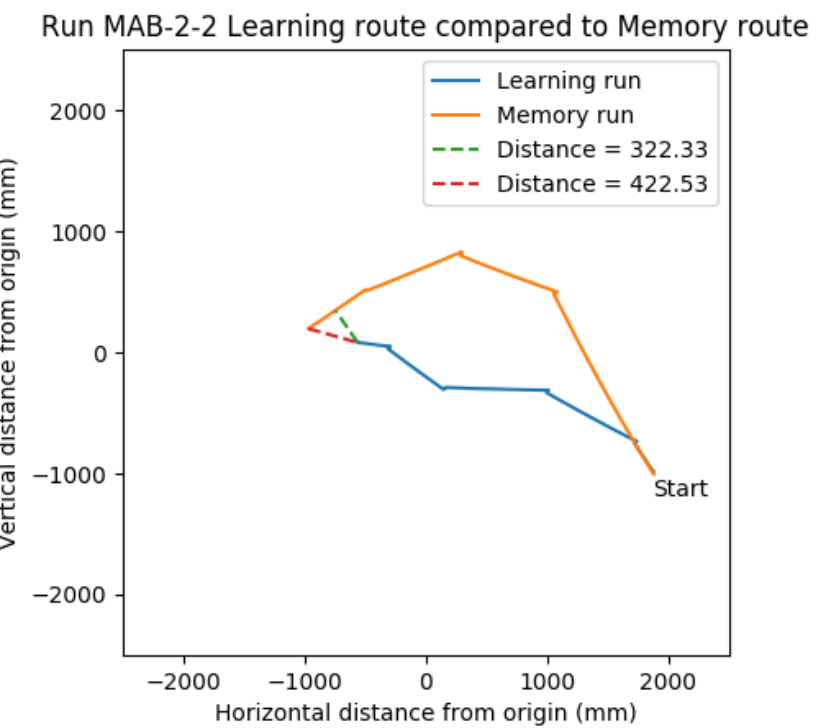


Figure 27: Trajectory plot of run AB-1-2; a near-successful recovery.

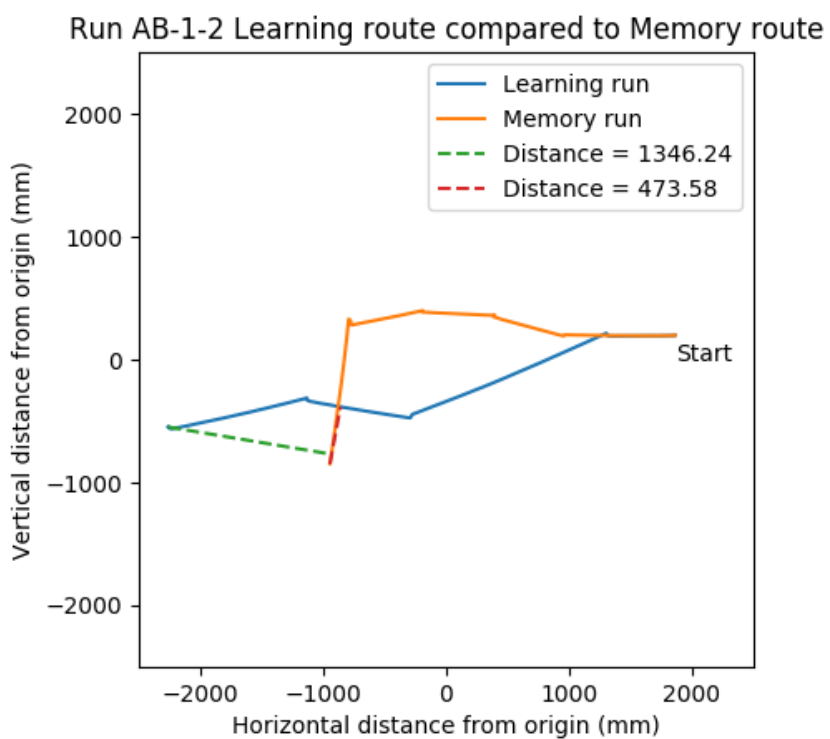


Figure 28: Trajectory plot of run AB-1-2; a failed recovery.

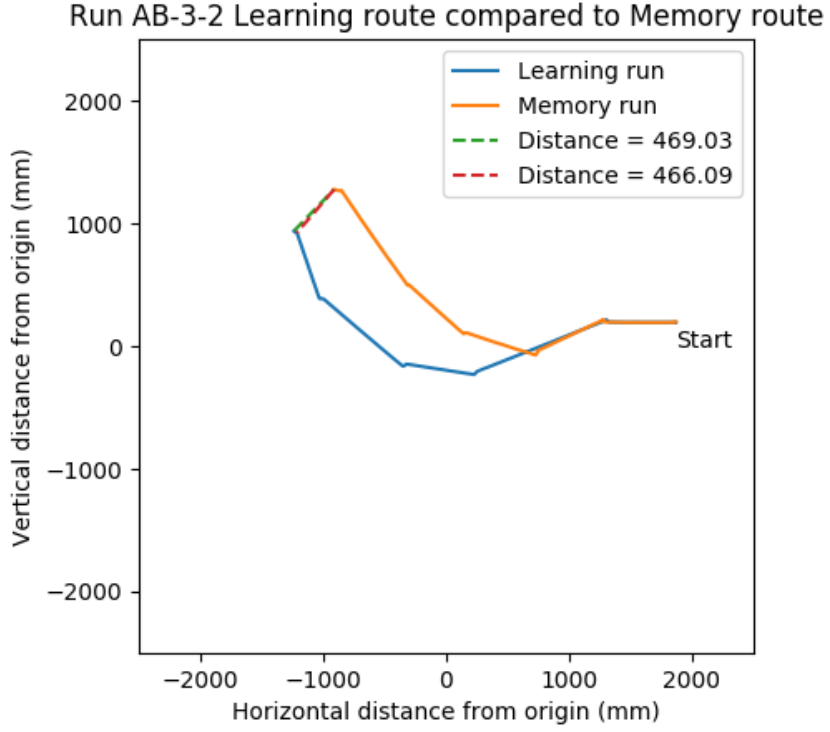


Figure 29: Trajectory plot of run AB-3-2.

In all, the visual navigation system performed quite well. Drastic errors were rare, though certainly present. The full series of trajectories in Appendix A show that the network was capable of reproducing routes on a robot through a cluttered, yet low detail, environment using a visual scanning route following behaviour.

The Homeward Experiment: What follows was not a formal experiment, but rather an exercise in curiosity. We gave AntBot the ability to learn homeward routes by rotating each image by 180° and storing both the original and rotated versions. The robot was then set to run a learning route through an empty arena and tasked with retracing its route home, then back out, and so on. Two experiments of this nature were conducted, however, only one was recorded. During the first experiment, the arena contained a box and the robot did not cope well with this landscape; outbound routes performed as well as could be expected, though inbound routes failed badly, requiring numerous corrections.

The second experiment (taking place in the empty arena) fared far better, though corrections were still required. This experiment was recorded and the trajectories can be seen in Figure 30. Two corrections were required through the course of this experiment during runs *Memory 1* and *Memory 5*. Both corrections occurred at an offset of greater than $2000mm$ (in the negative direction) from the origin and, once corrected, the robot successfully navigated home. The homeward route *Memory 3* required no correction.

These results indicate a significant improvement over the results presented by *Zhang* with regard to the scanning route following strategy and bring the performance more in line with the klinokinesis results presented in [17]. Previously, multiple errors were

Attempted recapitulation of out-bound (even),
and home-bound (odd) routes using image rotation

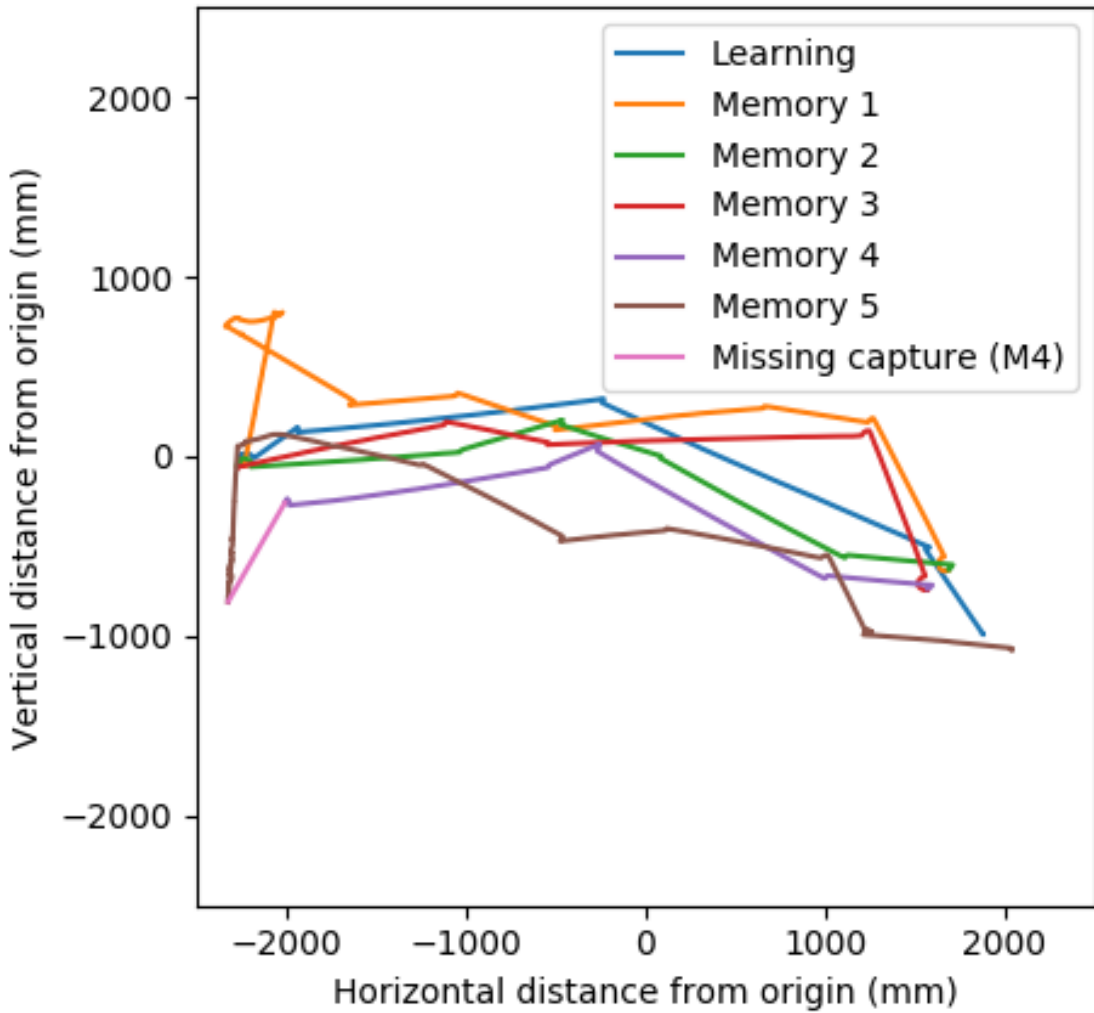


Figure 30: Trajectory plot of the homeward experiment. The Vicon capture was accidentally stopped early during outward trip *Memory 4* and the last section of the trip was missed. The linkage has been filled in to show where the rough route the robot took but it must be understood that this is not part of the recording, the line was simply drawn to fill in the gap.

experienced per run when using scanning, while our visual scanning behaviour demonstrated a much more stable performance replicating (albeit with varying degrees of success) 14 of 18 runs, only one of which experienced serious error, though it recovered. The homeward experiment experienced only two errors over the five memory runs.

7 Discussion

7.1 Conclusion

In this project, we have investigated the plausibility of a visual collision avoidance system based on optical flow combining this with a visual navigation model using the Mushroom Body. We investigated two different optical flow based collision avoidance systems and found results indicating the impracticality of a time-to-collision/depth centric system on the current robot. We also presented here results which show that even a basic flow filter based system can function well, though is certainly not without its flaws. We then investigated the Mushroom Body circuit for visual navigation, undertaking the debugging process to find out why the network seemingly did not function as it should. In the end, the problem with the visual navigation was found to be the route following strategy which was failing as a result of the control system implementation. We implemented a visual scanning algorithm for the robot and saw a drastic improvement in the functionality of the navigation system. Results presented for the Mushroom Body demonstrate a clear capacity for route memory in the context of a “visual corridor” allowing the robot to navigate in the manner observed in ants. While we have seen improvement in the performance of the MB model, we do still present many cases where the robot became confused, or chose its direction incorrectly. We will present ideas for future improvement in the following section.

7.2 Future work - Potential developments for MInf Part 2

7.2.1 Improvements on work presented

Here we wish to draw attention to the flaws in the experiments or research presented here and propose solutions as well as suggest potential future developments.

Time-to-Contact: Firstly, we wish to discuss time-to-contact and image depth. While the methods presented did not work, there are some modifications that could be made to gain a functioning system. We know that the system struggles to cope with a dense flow field, yet the points returned by the *goodFeaturesToTrack()* result in inconsistency. We could however take a subset of a dense flow field to reduce the computational demand, yet maintain the stability of considering set points in the frame. The flow field was not the only problem in computing time-to-contact. We also need the translational velocity of the camera. *Scimeca* found that a dense flow field was far better at computing accurate speed information than a sparse field, however, only one field may be in use on the robot at a single time. Introducing a subset system would allow us to use the dense flow information to compute the speed which gives us a more accurate estimation of time-to-contact. Alternatively, wheel encoders could be used to compute the distance and therefore speed information [16]. We would like to investigate this system further in Part 2, however, AntBot’s field of vision may cause problems for a depth centric system.

We note also that AntBot’s field of vision is distorted and while the tussocks may seem to completely fill the camera view, in reality, they are providing minimal detail. This could quite easily be remedied by constructing larger tussocks which provide more detail. We think that this could have a great effect on the performance of the VN and CA systems here presented.

Filtering: The filtering CA system certainly requires refinement. We have shown that it works and is plausible, but the implementation leaves a lot to be desired. Ideally we would like to see smooth, immediate responses to stimuli. A proportional response would be excellent, however, this presents a number of challenges from a hardware perspective which will be discussed in Section 7.2.2. It was noted earlier that such responses were too slow for the experimental environment, however, these methods were tested pre-upgrade. Turning methods with the new power supply were untested, however it is clear that the robot is capable of faster movement in general, so turning will be faster and may now be an option. For the same reason, klinokinesis may now be a viable route following strategy in a cluttered environment where it was not on the uptake of this project. We should note that visual collision avoidance, while interesting, is not crucial for insects as they have other mechanisms to help deal with this (e.g. antenna). We could integrate a simple mechanosensor to act as a backup in the case the visual system fails. Another aspect which could be examined is the choice of filter; the filter was chosen for simplicity, however, it would be interesting to experiment with something different. We think it unlikely that much time will be spent on this in Part 2, though it will be studied if time is available.

Visual Navigation: The results for the VN portion of this project are decent, though presenting them aptly has been challenging. While they certainly show promise for the model, there is no straightforward way to quantify the results. Saying “this route looks similar to this other route” is not a good way of presenting results. In part, this is due to the nature of the experiments, errors were not corrected as we wished to observe the agent’s behaviour and doing so meant stepping into the arena and corrupting AntBot’s view. However, it can be seen in Figure 30 that applying corrections to the robot did not result in a corrupted route as we feared it would and in fact could have produced more meaningful results.

One might suggest that we take some similarity metric such as the sum of squared error between the two routes, establishing an error threshold for what might be considered a success. In practice this is made difficult by the nature of the information returned by the Vicon system though it may not be impossible. The recordings are of different lengths and even removing duplicates (e.g. where the robot was sat still for multiple frames) does not result in frame x in the learning run corresponding to frame x in the memory run. Computing the distance between the points may not be the best method but it certainly gives something more tangible than the current results.

Another method, suggested by Dr. B. Webb, was to connect the two routes by computing a line from the end of the learning route to a close point on the memory route. We can then compute the area enclosed between the two routes and use this area as a metric for overall route similarity, in addition to the distances we presented as part of this work. However, this method fell victim to the same problem. Shading regions between curves in pyplot seems to rely on both curves having an equal number of points. Time was not available to investigate this further, though we would like to find a way to implement such a system during Part 2 of the project as we feel the data would prove very useful.

VN Extensions: One of the original goals for this project was to investigate the performance of a MB based navigational model which used real weightings for the KCs, as opposed to binary weightings. Code was written to model this, however, the model was never tested or used in experiments due to the difficulties in establishing a working baseline using the binary model, so we instead decided to focus on achieving that baseline. However, the real valued network could easily be put into use in future iterations of this project. We also included the capability for PN processing (normalisation) but this was not used for this project. Again, PN normalisation could easily be included in future projects and may provide better tolerance to changing conditions (e.g. changing light levels). The effects of these extensions will be examined in Part 2.

Future Experiments: Finally, the experimental scenario itself could be made far more complex. Admittedly, we aimed to demonstrate basic functionality of the visual navigation system in the real world using a scanning route following strategy, however, we have implementations of the Central Complex neural model as well as a method for combining both the CX and MB models to perform a joint navigational task [17, 11] present on the robot. The building blocks have been gradually placed over the last few years to allow for some interesting experiments to be conducted. A simple scenario was dreamt up early in this project but deemed impractical at the time; however, it may now be possible to build such a scenario. We set up an arena, similar to the ones used in our experiments though ideally larger. We define two locations in the arena to act as a food source and a nest then we use some abstract feedback system whereby the robot receives a signal to tell it that it has arrived at the food source or the nest. The robot can be sent on a foraging run from the nest until it finds the food source, storing path integration information as it goes. Upon finding the food source, the robot navigates back home using the path integration vector and collision avoidance learning the homeward route as it goes. It can then navigate back out via the PI vector and collision avoidance, learning the outbound route as it goes. The final stage is then to allow the robot to follow the learned visual routes. An extension, though this seems impractical on AntBot currently, could be to maintain a single instance of the navigational models over multiple environments to see if the robot can remember multiple different routes to food, rather than just a single route. This is presented as food-for-thought; due to the complexity it is unlikely that such a scenario could be studied during Part 2, however, we think it would be a good focus for a new project. We can use this scenario to set our own goals: We want the VN/CA systems as well as the hardware to be ready for such an experiment by the culmination of Part 2.

7.2.2 Engineering

Software: Here we wish to present future engineering suggestions regarding AntBot. The first thing that must be talked about is the codebase itself. As the code is inherited from three previous generations of the project it has become messy; combined with the process of learning to program in Android, as well as the fact that much of the existing code (admittedly, including our own) is poorly documented means that a significant amount of time during an AntBot project is likely to be spent getting to grips with the robot and the codebase. There is a straightforward, though horrendously time consuming fix in refactoring and documenting much of the code on AntBot. However, this solution also relies on each successor being familiar enough with Android to commit

to the system design. This should not be considered a deterrent as any system will have some kind of learning curve, however, it is important that any future system has sufficient documentation to allow students to pick up the project with relative ease. Operation of the robot should not present a major roadblock. Again, my thanks go to my predecessors who were more than willing to discuss the codebase and help me understand the system.

Hardware/Firmware: While AntBot is certainly a capable robot, the hardware does present some limitations. The two main issues are linked to robot control. Firstly, the command execution and synchronisation delays; commands require roughly 1 second of thread delay to execute and main loops require roughly 0.6 seconds of delay per iteration to keep everything in sync. For basic operation, this presents no problems, but a more refined control system (from the Android component) is made difficult and accurate timing in threads becomes impossible. Reactionary behaviours will work at times, but ultimately the delays cause a delayed reaction (one of the main reasons the stop-then-turn behaviour was added to the learning runs for VN experiments). The only known way around this is to construct arenas in such a manner that the robot has additional time to cope with the delays. The synchronisation delays cause timing issues; however, omitting them causes the application to slow drastically. These are necessary by design.

The only other platform problem is the firmware on the Arduino which can easily be re-written. The firmware architecture is entirely appropriate but the control code needs re-written and possibly a sensor added. This became apparent during initial tests with the robot, wherein equal speeds to both sides using the *go* command would result in a curved trajectory. As ever with wheeled robots, one side has slightly better drive than the other, however, this should be dealt with at a firmware level, the left side always requires approximately 90% the power of the right, so we can modify the motor commands at a firmware level to reflect this. The turning is also very inaccurate which was noted in early scanning tests, and the later homeward experiment. The turning code is based purely based on encoder values, and while there is nothing wrong with this method in theory, in practice it results in the robot running over, or under (due to slippage) the desired angle. A simple PID control system using a gyroscope or compass could remove this problem entirely. Motor speeds were also power dependent, so a voltage regulator would be a nice addition to ensure experiments remain consistent at varying power levels. We aim to start MInf Part 2 by addressing this aspect of the robot.

In this project, we discovered just how seriously simple hardware and control problems can affect the performance of otherwise good models. As we are interested in the models, control should be implemented using whatever sensors are necessary. The key point is that the models themselves must only operate on visual information.

8 References

- [1] The brain of the honeybee *apis mellifera*. i. the connections and spatial organization of the mushroom bodies. *Philosophical Transactions of the Royal Society of London B: Biological Sciences*, 298(1091):309–354, 1982.
- [2] Paul Ardin, Fei Peng, Michael Mangan, Konstantinos Lagogiannis, and Barbara Webb. Using an insect mushroom body circuit to encode route memory in complex natural environments. *PLOS Computational Biology*, 12(2):1–22, 02 2016.
- [3] Bart Baddeley, Paul Graham, Philip Husbands, and Andrew Philippides. A model of ant route navigation driven by scene familiarity. *PLOS Computational Biology*, 8(1):1–16, 01 2012.
- [4] Laura Dittmar, Wolfgang Stürzl, Emily Baird, Norbert Boeddeker, and Martin Egelhaaf. Goal seeking in honeybees: matching of optic flow snapshots? *Journal of Experimental Biology*, 213(17):2913–2923, 2010.
- [5] O.P. Buneman D.J. Willshaw and H. C. Longuet-Higgins. Non-holographic associative memory. *Nature*, 1969.
- [6] Leonard Eberding. Development and Testing of an Android-Application-Network based on the Navigational Toolkit of Desert Ants to control a Rover using Visual Navigation and Route Following., 2016.
- [7] Aleksandar Kodzhabashev. Roboant: Build your own android robot, 2014. <https://blog.inf.ed.ac.uk/insectrobotics/roboant/> (*Last visited 22/01/2018*).
- [8] Aleksandar Kodzhabashev and Michael Mangan. Route following without scanning. In Stuart P. Wilson, Paul F.M.J. Verschure, Anna Mura, and Tony J. Prescott, editors, *Biomimetic and Biohybrid Systems*, pages 199–210, Cham, 2015. Springer International Publishing.
- [9] Toby Low and Gordon Wyeth. Obstacle detection using optical flow. In *in Proceedings of the 2005 Australasian Conf. on Robotics & Automation*, 2005.
- [10] Peter O'Donovan. Optical flow: Techniques and applications. 2005.
- [11] Luca Scimeca. AntBot: A biologically inspired approach to Path Integration, 2017.
- [12] Kahlouche Souhila and Achour Karim. Optical flow based robot obstacle avoidance. *International Journal of Advanced Robotic Systems*, 4(1):2, 2007.
- [13] Finlay J. Stewart, Dean A. Baker, and Barbara Webb. A model of visual–olfactory integration for odour localisation in free-flying fruit flies. *Journal of Experimental Biology*, 213(11):1886–1900, 2010.
- [14] Rüdiger Wehner. The architecture of the desert ant's navigational toolkit (hymenoptera: Formicidae). *Myrmecological News*, 12:85–96, 09 2009.
- [15] Rüdiger Wehner, Martin Boyer, Florian Loertscher, Stefan Sommer, and Ursula Menzi. Ant navigation: One-way routes rather than maps. *Current Biology*, 16(1):75 – 79, 2006.
- [16] Matthias Wittlinger, Rüdiger Wehner, and Harald Wolf. The ant odometer: Stepping on stilts and stumps. *Science*, 312(5782):1965–1967, 2006.

- [17] Zhaoyu Zhang. Developing AntBot: a mobile-phone powered autonomous robot based on the insect brain, 2017.

A Visual Navigation trajectory plots

A.1 AB Runs

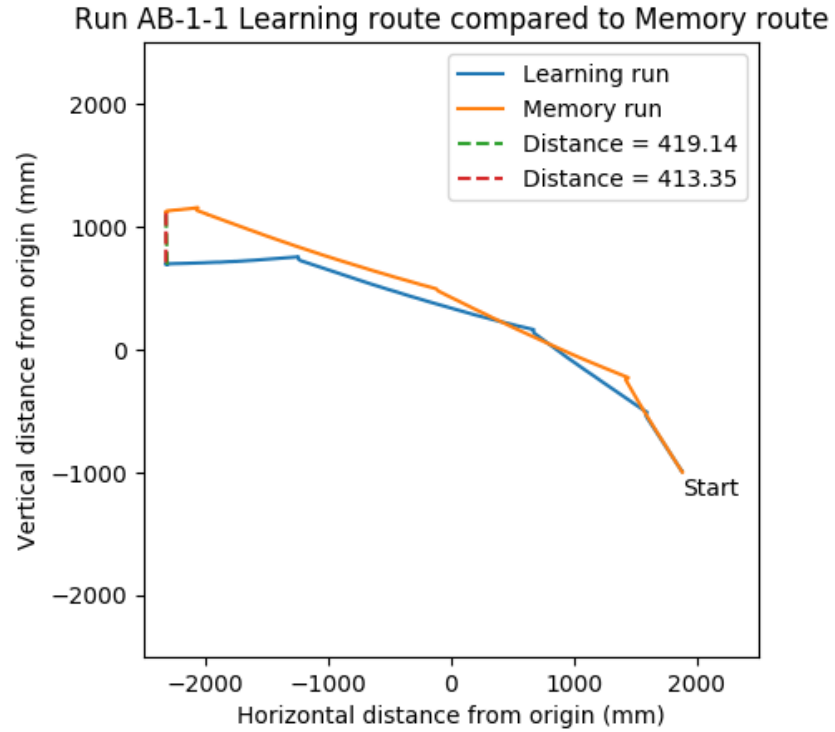


Figure 31: Run AB-1-1.

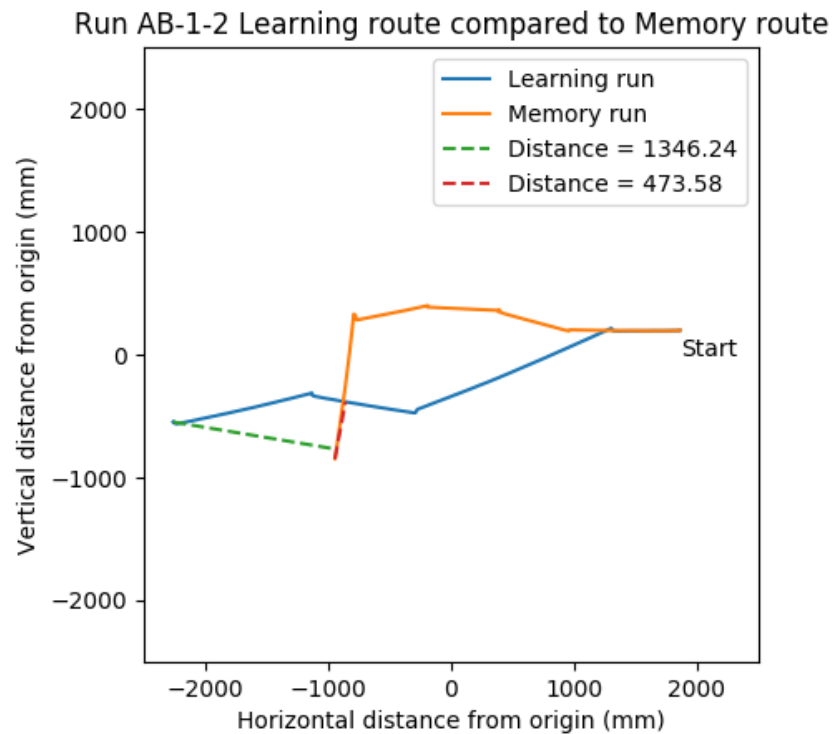


Figure 32: Run AB-1-2.

Run AB-2-1 Learning route compared to Memory route

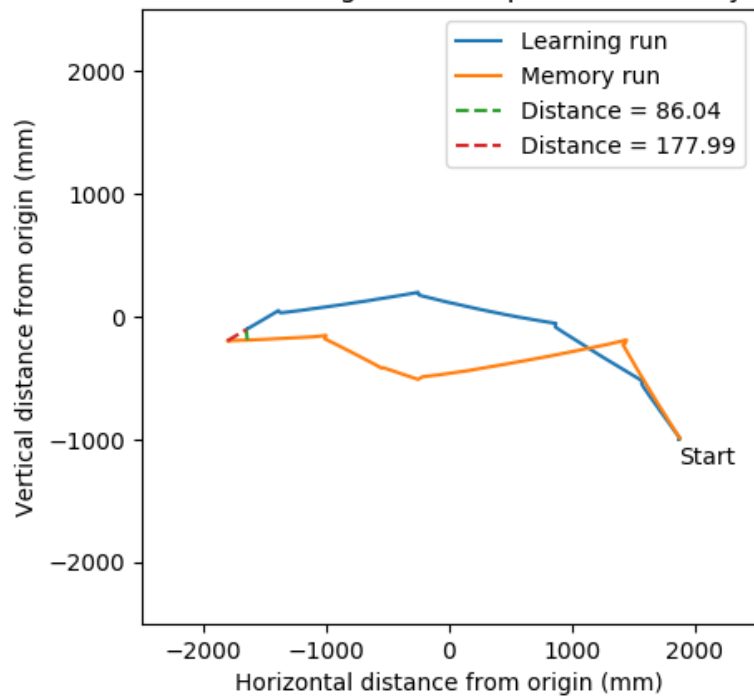


Figure 33: Run AB-2-1.

Run AB-2-2 Learning route compared to Memory route

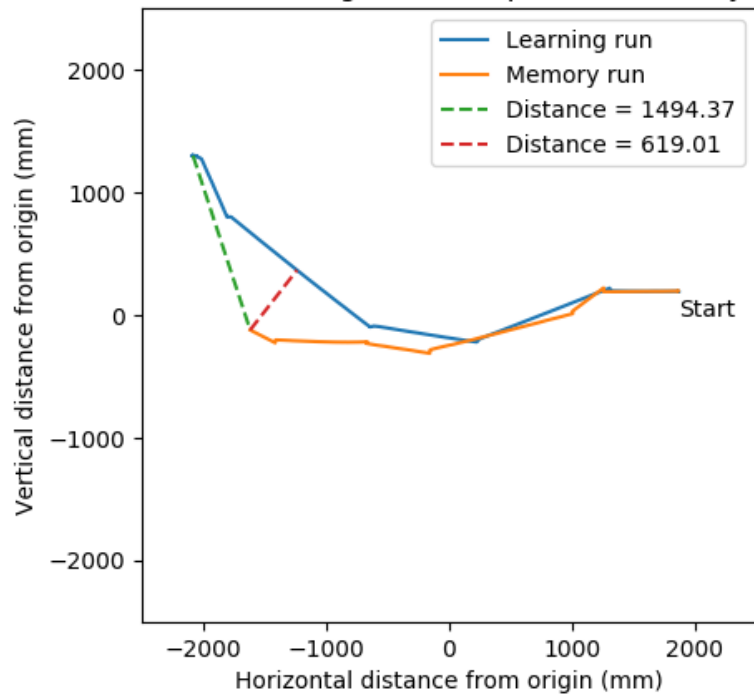


Figure 34: Run AB-2-2.

Run AB-3-1 Learning route compared to Memory route

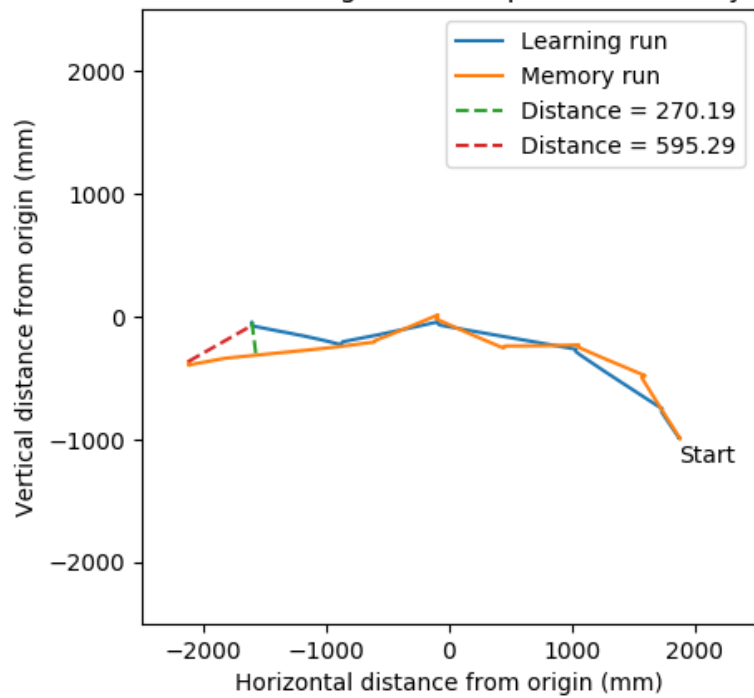


Figure 35: Run AB-3-1.

Run AB-3-2 Learning route compared to Memory route

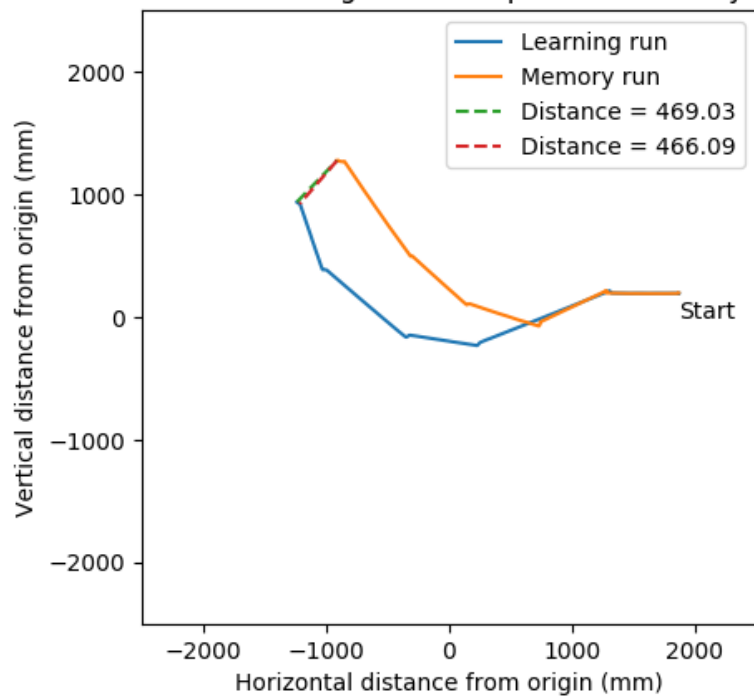


Figure 36: Run AB-3-2.

Run AB-4-1 Learning route compared to Memory route

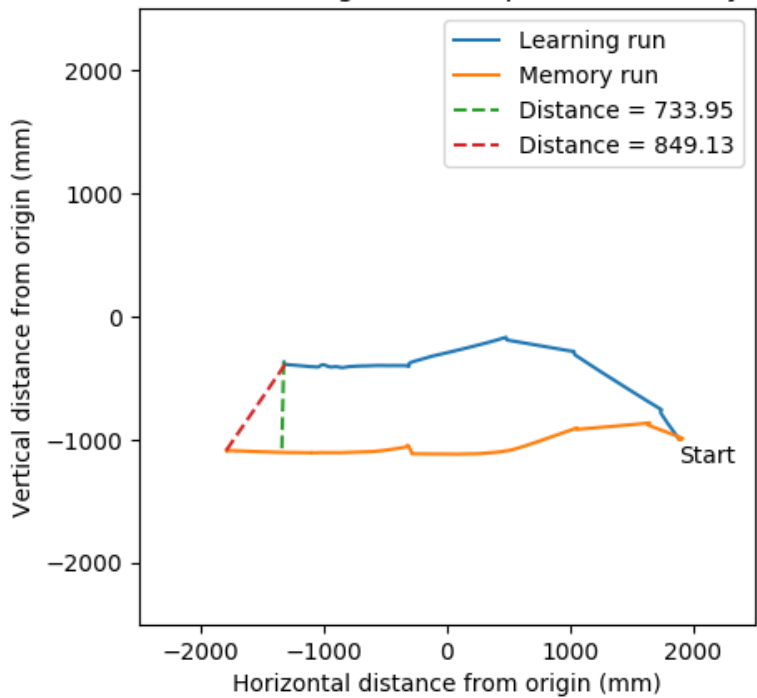


Figure 37: Run AB-4-1.

Run AB-4-2 Learning route compared to Memory route

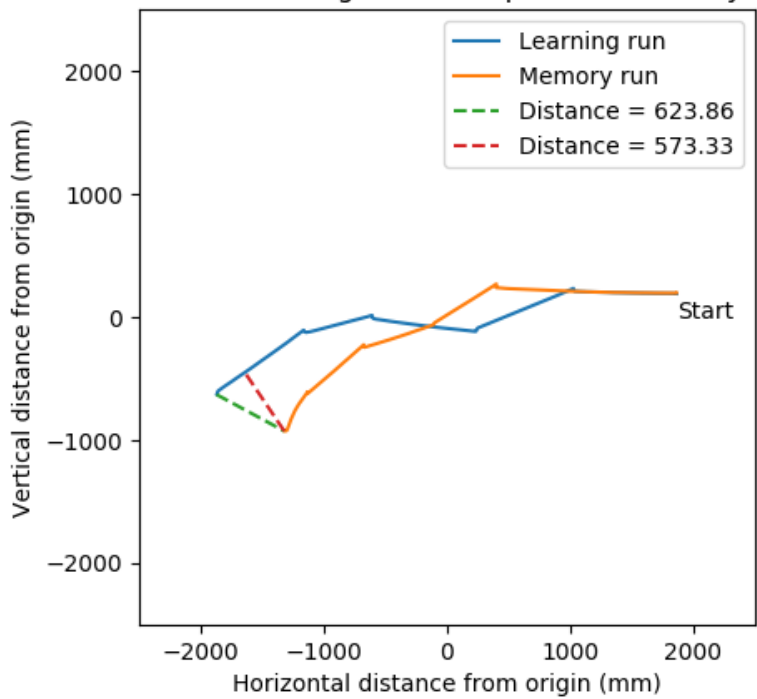


Figure 38: Run AB-4-2.

A.2 MAB Runs

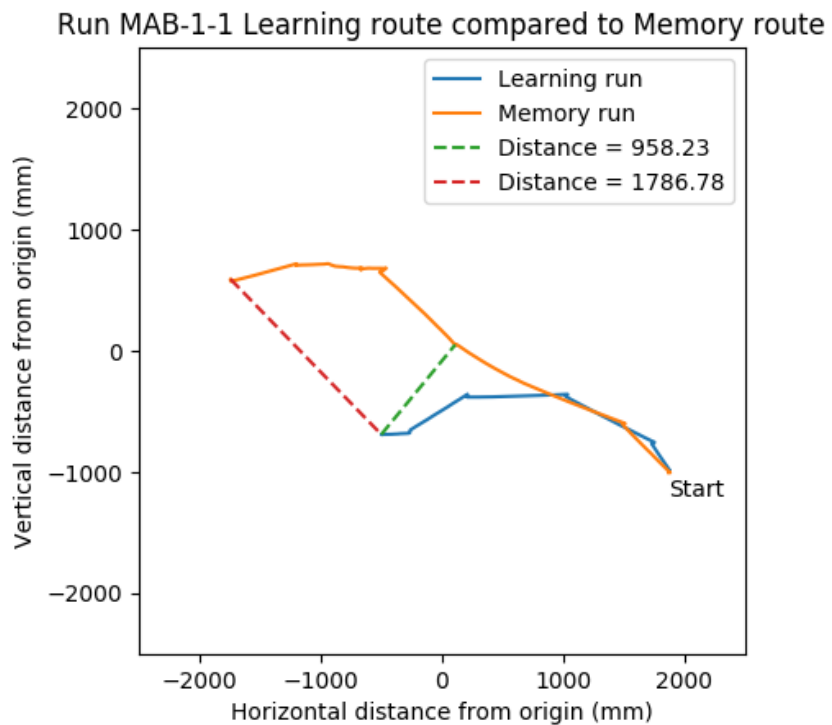


Figure 39: Run MAB-1-1.

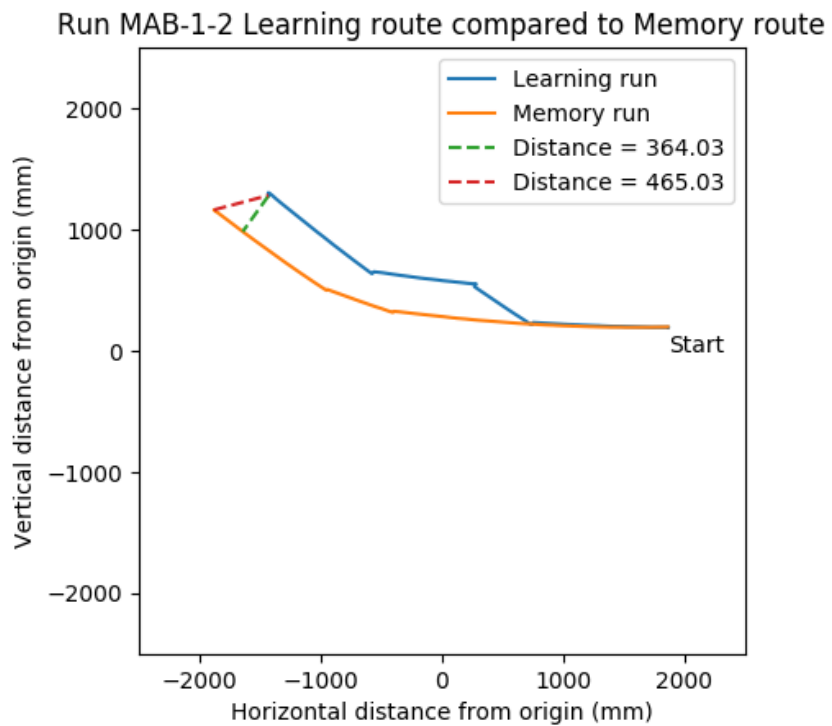


Figure 40: Run MAB-1-2.

Run MAB-2-1 Learning route compared to Memory route

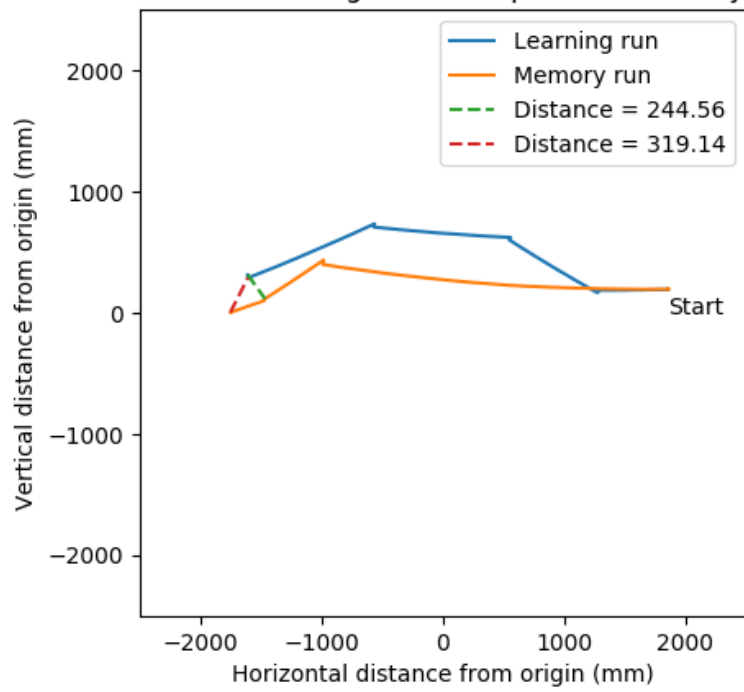


Figure 41: Run MAB-2-1.

Run MAB-2-2 Learning route compared to Memory route

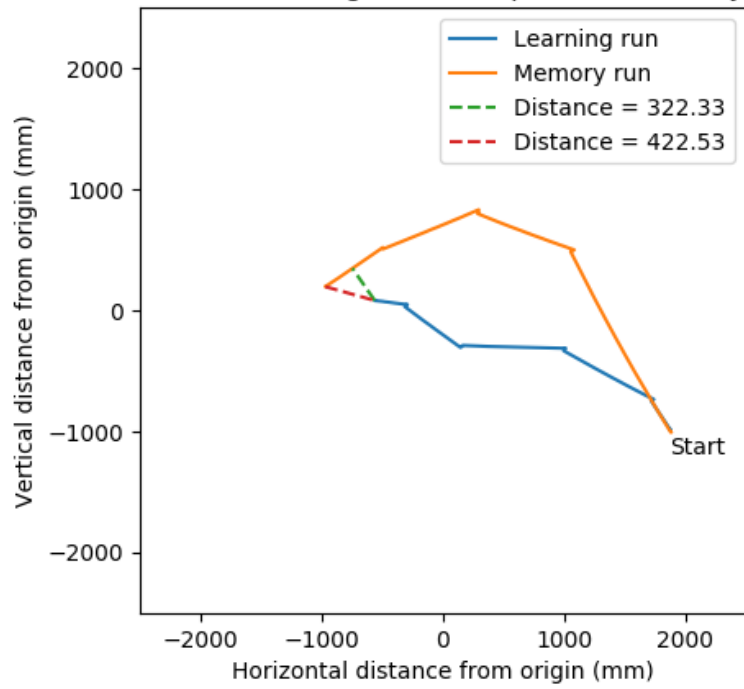


Figure 42: Run MAB-2-2.

Run MAB-3-1 Learning route compared to Memory route

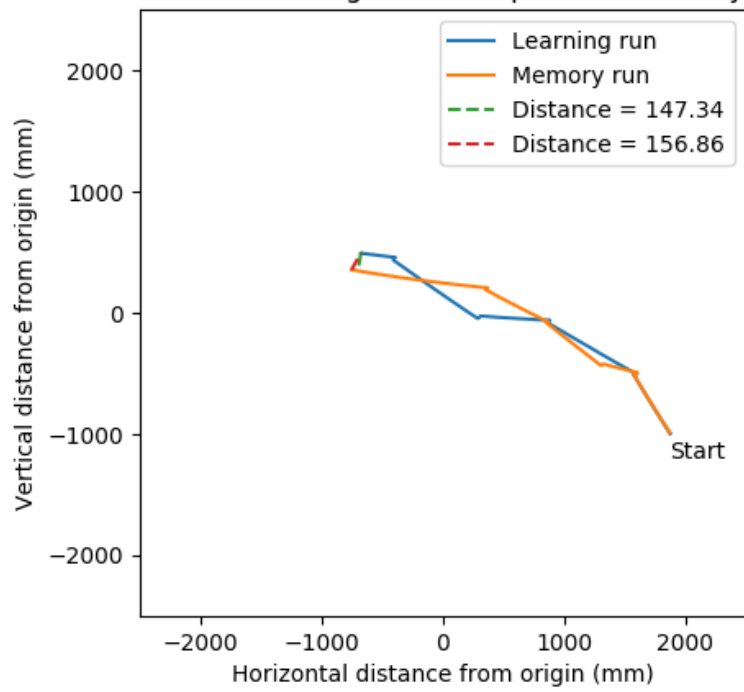


Figure 43: Run MAB-3-1.

Run MAB-3-2 Learning route compared to Memory route

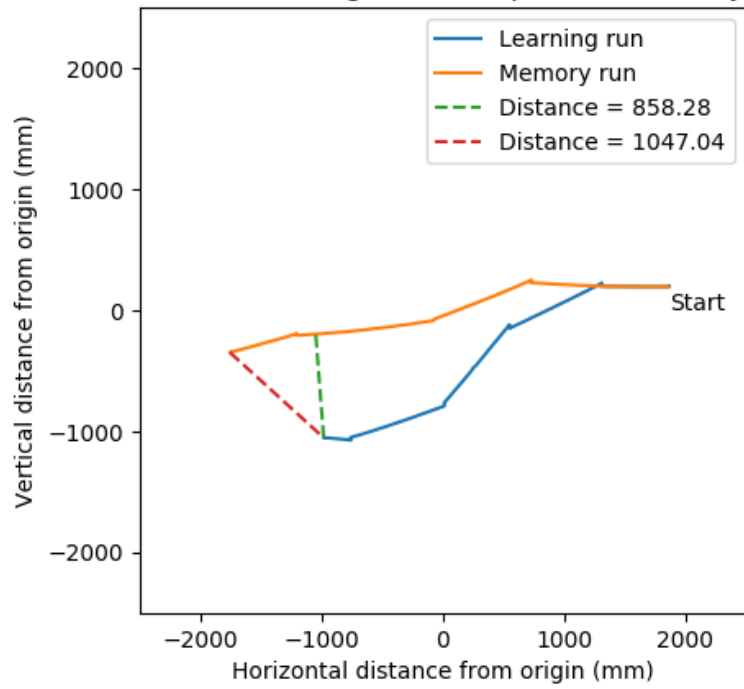


Figure 44: Run MAB-3-2.

Run MAB-4-1 Learning route compared to Memory route

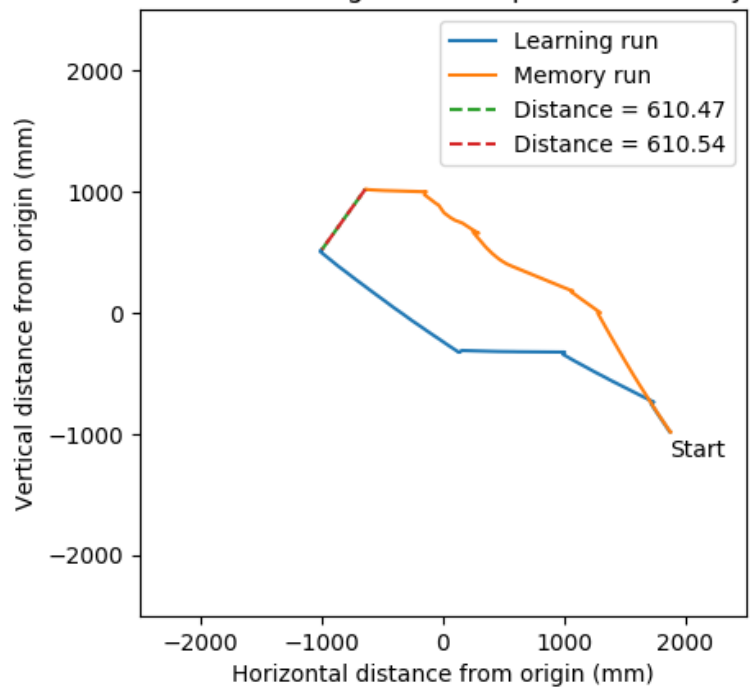


Figure 45: Run MAB-4-1.

Run MAB-4-2 Learning route compared to Memory route

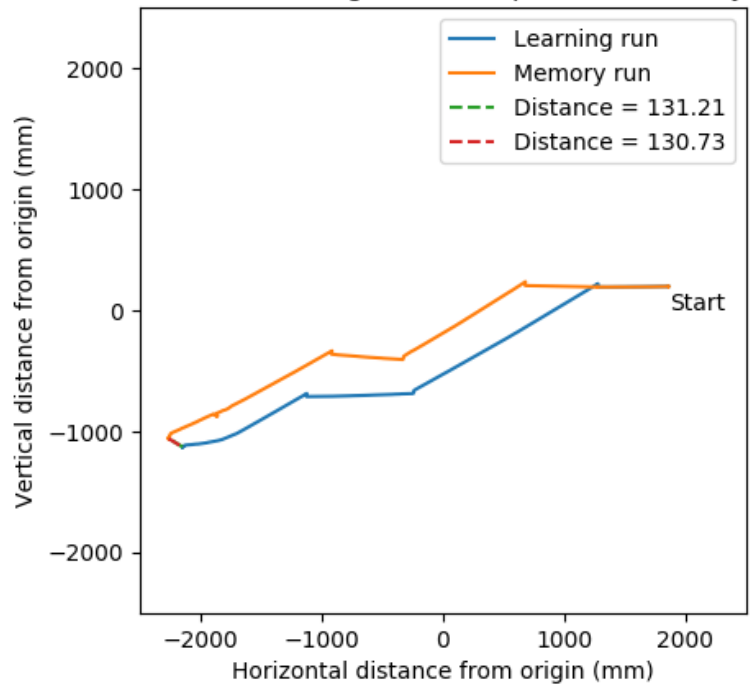


Figure 46: Run MAB-4-2.

Run MAB-5-1 Learning route compared to Memory route

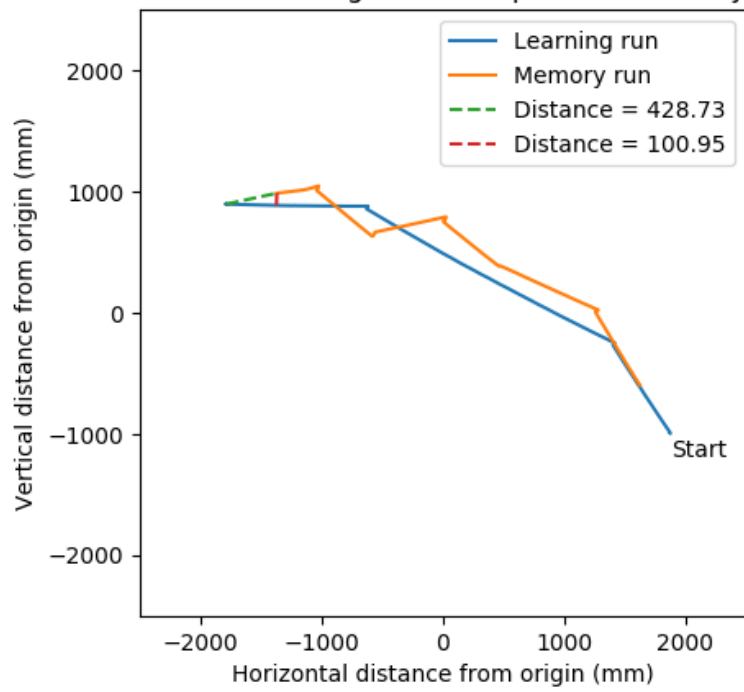


Figure 47: Run MAB-5-1.

Run MAB-5-2 Learning route compared to Memory route

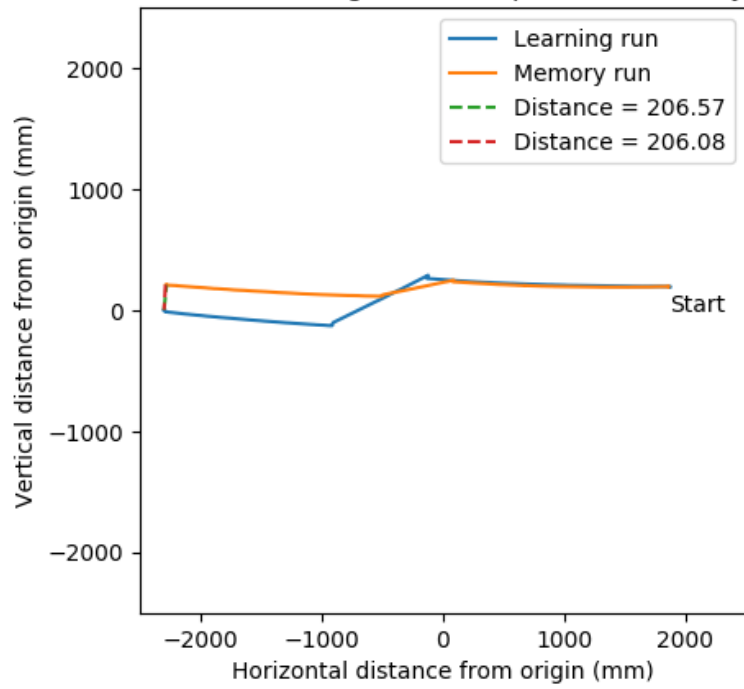


Figure 48: Run MAB-5-2.